Downloaded from orbit.dtu.dk on: Apr 28, 2024

DTU Library

# 3D shape optimization of loudspeaker cabinets for uniform directivity

**Andersen, Peter Risby; Cutanda Henríquez, Vicente; Aage, Niels; Kook, Junghwan**

*Published in:*
Structural and Multidisciplinary Optimization

*Link to article, DOI:*
10.1007/s00158-022-03451-2

*Publication date:*
2022

*Document Version*
Peer reviewed version

Link back to DTU Orbit

*Citation (APA):*
Andersen, P. R., Cutanda Henríquez, V., Aage, N., & Kook, J. (2022). 3D shape optimization of loudspeaker cabinets for uniform directivity. *Structural and Multidisciplinary Optimization*, *65*(12). https://doi.org/10.1007/s00158-022-03451-2

**General rights**
Copyright and moral rights for the publications made accessible in the public portal are retained by the authors and/or other copyright owners and it is a condition of accessing publications that users recognise and abide by the legal requirements associated with these rights.

- Users may download and print one copy of any publication from the public portal for the purpose of private study or research.
- You may not further distribute the material or use it for any profit-making activity or commercial gain
- You may freely distribute the URL identifying the publication in the public portal

If you believe that this document breaches copyright please contact us providing details, and we will remove access to the work immediately and investigate your claim.

**Noname manuscript No.**
(will be inserted by the editor)

# 3D shape optimization of loudspeaker cabinets for uniform directivity

**Peter Risby Andersen · Vicente Cutanda Henríquez · Niels Aage · Junghwan Kook**

Received: date / Accepted: date

**Abstract** This paper presents a method to perform gradient-based shape optimization to minimize the root mean square deviation of the exterior acoustic sound pressure level distribution in front of an initially spherically-shaped loudspeaker. The work includes several examples of how different multi-frequency optimization strategies can affect the final optimized design performance. This includes testing, averaging and weighting of multi-frequency cost functions or using a minimax formulation. The shape optimization technique is based on an acoustic Boundary Element Method coupled to a Lumped Parameter loudspeaker model. To control and alter the deformation of the loudspeaker cabinet the optimization method adapts a spherical free-form deformation approach based on Bernstein polynomials. For the particular optimization problems presented, it is shown that improvements in the root mean square deviation of the sound pressure level in front of the loudspeaker can be achieved between 1 kHz and 5 kHz. In the best case scenario, less than a 1 dB Sound Pressure Level (SPL) variation is observed between on-axis and a 70 degrees off-axis response in the range 2 to 5 kHz. The widest frequency bandwidth and smoothest response of the root mean square deviation is found by utilizing the minimax formulation.

**Keywords** acoustics · loudspeakers · shape optimization · adjoint sensitivities · boundary element method

Peter Risby Andersen
GN Audio A/S & Jabra, Audio Research, Lautrupbjerg 7, 2750 Ballerup, Denmark
E-mail: prandersend@jabra.com

Vicente Cutanda Henríquez
Centre for Acoustic-Mechanical Micro Systems, Department of Electrical and Photonics Engineering, Technical University of Denmark
Ørsteds Plads, Building 352, DK-2800, Kgs. Lyngby, Denmark
E-mail: vcuhe@dtu.dk

Niels Aage
Centre for Acoustic-Mechanical Micro Systems, Department of Civil and Mechanical Engineering, Technical University of Denmark
Koppels Allé, Building 404, DK-2800, Kgs. Lyngby, Denmark
E-mail: naage@mek.dtu.dk

Junghwan Kook (corresponding author)
GN Audio A/S & Jabra, Audio Research, Lautrupbjerg 7, 2750 Ballerup, Denmark
E-mail: jkook@jabra.com

## 1 Introduction

The development of moving coil loudspeaker systems has undergone gradual improvements for more than 100 years. Traditionally, engineering and mathematical modeling of loudspeakers has been relying on simplified lumped parameter models e.g using equivalent circuit theory (Small, 1971; Leach, 2010). Over the last two decades, the increase in computational power has allowed research and development of loudspeakers to transition to more complex and accurate numerical modeling methods, such as the Finite Element Method (FEM) or the Boundary Element Method (BEM) (Wright, 1998; Juul-Nyholm et al., 2017; Panzer, 2012). This has driven the trend of making loudspeaker systems increasingly smaller while maintaining high audio quality. A trend that is e.g. seen in the development of smartspeakers, speakerphones and smartphones.

Nevertheless, application of methods like FEM and BEM to improve the acoustic performance still requires the operating engineer to make the appropriate design changes. This is a task that will typically be based on a

trial and error approach combined with the experience of the engineer. Optimization methods can potentially further aid this design process. There are several examples of optimization being applied to acoustic problems. Especially, the optimization of horn loudspeakers has been studied. Udawalpola et. al. use gradient-based shape optimization to improve the radiation efficiency of a horn relying on an axisymmetric BEM with continuous adjoint sensitivities, and also FEM based shape optimization including the far-field directivity as part of the cost function (Udawalpola et al., 2011; Udawalpola and Berggren, 2008). Similarly, Bängtsson et. al. perform shape optimization of a 2D version of an acoustic horn for reduced reflection over a frequency band (Bängtsson et al., 2003). In a more recent publication, Schmidt et. al. show a 3D large-scale broadband acoustic shape optimization approach utilizing a time-domain discontinuous Galerkin method to improve the impedance matching of an acoustic horn (Schmidt et al., 2016). Also, Khajah et. al. recently showed how a 2D Scaled Boundary Finite Element Method can be used to efficiently shape optimize acoustic horns, and also apply it to optimize acoustic metamaterial (Khajah et al., 2021).

Besides the optimization of horns, optimization methods are also being applied to loudspeaker design. Christensen et. al. shape optimize a loudspeaker unit for improved sound directivity using an axisymmetric BEM description of the loudspeaker and finite difference sensitivities (T. Christensen and Olhoff, 1998). Bezzola shows how loudspeaker elements can be optimized using both parameter, shape, and topology optimization (Bezzola, 2018). Similarly, Christensen gives examples of how several components of loudspeakers, such as the motor system, the basket, heat sinks, or tweeter phase plugs, can be optimized using both shape and topology optimization (Christensen, 2020).

Recently, Nielsen et. al., based on an axisymmetric vibroacoustic FEM formulation, showed how broadband material optimization can be utilized to distribute materials of different properties in the loudspeaker diaphragm and surround to improve the flatness of the frequency response and the directivity pattern (Nielsen et al., 2021). Examples of the application of vibroacoustic optimization strategies for large-scale hearing instruments also exist, e.g. using parameter optimization combined with model reduction methods (Creixell Mediante et al., 2018) and more elaborate level-set based shape optimization (Dilgen et al., 2021; Dilgen and Aage, 2021).

The numerical acoustic optimization examples listed above have mainly investigated flat frequency response, radiation efficiency, and directivity responses. However, often the evaluation of loudspeaker systems is based on perceptual tests to understand their behavior in terms of sound quality. Nevertheless, there is a certain consensus that measures like flat frequency (Bücklein, 1981; Kates, 1979) or even power response (Linkwitz, 2002), and directivity (Evans et al., 2009; Queen, 1979) are important perceptual measures of what constitutes a good sounding loudspeaker.

In this work, a method is developed that is used to optimize and control the directivity pattern of a loudspeaker by changing the external shape of a loudspeaker cabinet. The external shape of the cabinet is controlled by using the Free Form Deformation (FFD) parametrization method (Sederberg, 1986) in spherical coordinates. Digital Signal Processing (DSP) has made it possible to more accurately control the frequency response flatness, therefore, the directivity pattern is chosen as a measure of the loudspeaker performance as DSP cannot control the directivity if only one loudspeaker is used. Moreover, compact loudspeaker systems such as smartspeakers and speakerphones are typically used in environments where the listening position is not necessarily stationary and therefore a more omnidirectional response is typically desirable. The developed shape optimization procedure will be based on a quarter symmetric BEM to model the exterior acoustic field. The structural, electrical, and interior acoustics components of the loudspeaker are considered through coupling to a lumped parameter model (LPM). Using a LPM is a common approach to reduce the model complexity which is desirable when performing optimization based on an otherwise relatively expensive numerical model (Panzer, 2012; Nielsen et al., 2020, 2021). The optimization method is tested on a representative idealized setup where the loudspeaker cabinet has a spherical shape. Several configurations of the cost function and multi-frequency optimization approaches are tested and evaluated. It should be noted that the presented work is a extension of previously presented work by the authors in a conference paper (Andersen et al., 2021).

The paper is organized as follows: first, the underlying numerical modeling approach using a quarter symmetric BEM coupled to a lumped parameter model is introduced. This is followed by sections describing the spherical loudspeaker test case, the parametrization of the speaker geometry, and the formulation of the shape optimization problem. Hereafter, several shape optimization results are shown for multiple optimiza-

tion settings. Finally, the results are discussed and conclusions are drawn.

## 2 The Boundary Element Method with symmetry conditions

Isentropic wave propagation can be described in the frequency domain using the time-harmonic Helmholtz equation (Kinsler, 2000)

$$\Delta p + k^2 p = 0 \quad \text{in} \quad \Omega, \tag{1}$$

where $p$ is the complex acoustic pressure perturbation, $k$ is the wavenumber and $\Omega$ represents the computational domain. The Helmholtz equation is typically solved by applying Dirichlet, Neumann or Robin conditions. In the following only Neumann boundary conditions are considered, meaning that

$$\frac{\partial p}{\partial n} = -i\omega\rho u_n \quad \text{on} \quad \Gamma, \tag{2}$$

where $\frac{\partial p}{\partial n}$ is the normal derivative of the pressure with respect to the boundary $\Gamma$. Additionally, $u_n$ is the normal velocity at $\Gamma$, $\omega$ is the angular frequency and $\rho$ is the density of air. Eq. (2) is known as Euler's equation. The exterior acoustic domain is solved by transforming the time-harmonic Helmholtz equation into the Kirchhoff-Helmholtz integral form, given by (Wu, 2000)

$$\begin{aligned} C(P)\, p(P) = &\int_\Gamma \frac{\partial G(R)}{\partial n} p(Q) \mathrm{d}\Gamma(Q) \\ &- \int_\Gamma G(R) \frac{\partial p(Q)}{\partial n} \mathrm{d}\Gamma(Q), \end{aligned} \tag{3}$$

where $R = \|P - Q\|$ is the distance between a collocation point $P_j$ and a point on the generator $Q$. Moreover, $C(P)$ and $p(P)$ are the integral-free term and the acoustic pressure at $P$, respectively. For smooth geometries, the integral-free term is either $2\pi$ on a boundary or $4\pi$ in the domain. However, for boundary elements utilizing typical continuous Lagrange polynomials the integral-free term is calculated using the approach in Ref. (Seybert et al., 1985). The integration is carried out over the surface $\Gamma$ and the Green's function $G(R)$ is defined as,

$$G(R) = \frac{e^{-\mathrm{i}kR}}{R}. \tag{4}$$

The following studies will use a quarter symmetric description of the geometry. Hence, the Kirchhoff-Helmholtz integral is re-written in the form

$$\begin{aligned} C(P_j)\, p(P_j) = &\int_\Gamma \frac{\partial G_s}{\partial n} p(Q) \mathrm{d}\Gamma(Q) \\ &- \int_\Gamma G_s \frac{\partial p(Q)}{\partial n} \mathrm{d}\Gamma(Q), \end{aligned} \tag{5}$$

with the Green's function $G_s$ contain contributions from the mirrored collocation points. Hence, the total Green's function is expressed as

$$G_s = \sum_{j=1}^{N_s} G(P_j, Q), \tag{6}$$

where $N_s = 4$ is the number of mirrored collocation points including the collocation point located on the meshed part of the geometry. Discretization of Eq. (5), applying the collocation method and Euler's equation yields the system of equations given by

$$\mathbf{A}\mathbf{p} + i\omega\rho\mathbf{B}\mathbf{u}_n = 0, \tag{7}$$

where $\mathbf{u}_n$ and $\mathbf{p}$ are vectors containing the surface normal particle velocity and the acoustic pressure at each node, respectively. Moreover, $\rho$ is the density of air, $\mathbf{B}$ and $\mathbf{A}$ are dense matrices containing the contributions from the single and the double layer potentials, respectively. The matrix $\mathbf{A}$ also includes the contribution from the integral-free term in the diagonal. Notice that Eq. (7) is undetermined in its current form, and that proper boundary or coupling conditions must be applied to either eliminate the velocity degrees of freedom or to couple them to an auxilliary set of equations. Therefore, the system is solved through coupling to a lumped parameter model at the loudspeaker unit and zero velocity boundary conditions elsewhere. The coupling procedure is described in the following section. The BEM matrices are assembled in a compiled MATLAB MEX/C++ environment and parallized using OpenMP. It should be noted that the assembly and kernel integration routine is very inspired by the approach found in the MATLAB based BEM library OpenBEM (Juhl and Henríquez, 2010). Furthermore, the matrices in Eq. (7) are assembled using the square matrix Combined Helmholtz Integral Equation Formulation (CHIEF) found in Ref. (Marburg and Nolte, 2008, Chapter 15) to circumvent irregular frequencies.

## 3 Lumped parameter loudspeaker model

Fully coupled structural, acoustic and electromagnetic numerical simulations of the entire loudspeaker system are very computationally costly, especially for three dimensional simulations. A method to reduce the computational cost of the loudspeaker modelling is to use a lumped parameter model (LPM) of the loudspeaker unit and couple it to the exterior BEM domain Beranek and Mellow (2012). The equivalent circuit of such approach is depicted in Figure 1. It should be noted that

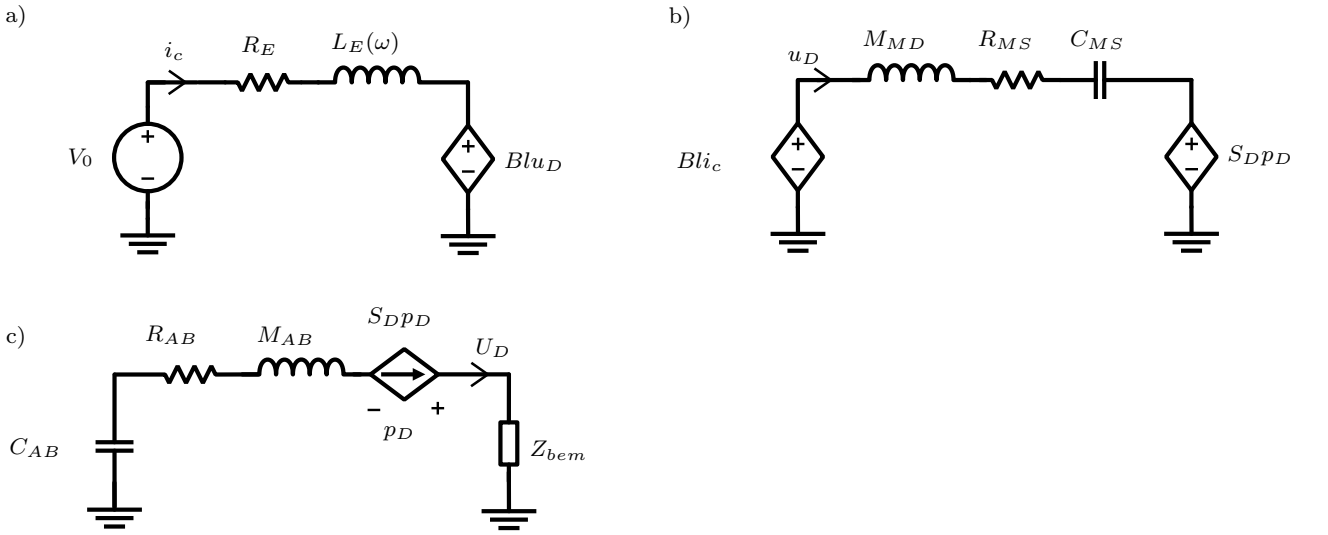


Fig. 1: Lumped parameter model of a closed-box loudspeaker coupled to exterior acoustic BEM. In the figure, a) shows the electrical components of the loudspeaker modelling the voice coil. Figure b) shows the mechanical parts of the loudspeaker that models the membrane, the spider and the suspension. In c) the internal acoustics of the closed-box is modelled with $C_{AB}$, $R_{AB}$ and $M_{AB}$. The lumped model is coupled to the BEM via the impedance $Z_{bem}$. The resulting fully coupled system of equations is given in Eq. (15).

the LPM is based on a low-frequency assumption and the mechanical system is limited by the cone break-up frequency and acoustic resonances inside the cabinet. The electrical, mechanical and acoustic cabinet impedance's, $Z_E$, $Z_{MD}$ and $Z_{AB}$ are given by

$$Z_E = R_E + L_E(\omega) \tag{8}$$

$$Z_{MD} = i\omega M_{MD} + R_{MS} + (i\omega C_{MS})^{-1}\,, \tag{9}$$

$$Z_{AB} = i\omega M_{AB} + R_{AB} + (i\omega C_{AB})^{-1}\,, \tag{10}$$

respectively. Where $R_E$ is the DC resistance, $L_E(\omega)$ is the frequency dependent voice coil inductance, $M_{MD}$ is the mechanical mass of the diaphragm and voice coil, $R_{MS}$ is the mechanical loss in the suspension and the voice coil, $C_{MS}$ is the mechanical suspension compliance, $M_{AB}$ is the acoustic mass of the enclosure, $R_{AB}$ is the energy dissipation resistance due to filling material and $C_{AB}$ is the compliance of the enclosure.

The BEM is coupled to the LPM by expressing the average acoustic BEM pressure solution in terms of an acoustic impedance. This assumes piston motion of the diaphragm and that the acoustic pressure acting in the direction of the diaphragm motion can be obtained from the average pressure across the diaphragm. The acoustic impedance seen from the BEM therefore becomes

$$Z_{bem} = \frac{p_{avg}}{U_D} = \frac{1}{S_D^2 u_D}\int_{\Gamma_D} p\, n_z d\Gamma_D, \tag{11}$$

where $\Gamma_D$ is the surface of the loudspeaker, $U_D$ is the volume velocity of the loudspeaker diaphragm, $p_{avg}$ is the average pressure on the diaphragm acting in the direction of loudspeaker movement, $S_D$ is the effective surface area of the diaphragm, $n_z$ is the z-component of the surface normal vector and $u_D$ is a scalar value describing the velocity of the diaphragm. Combining the impedance's and transforming the acoustic quantities into the mechanical domain by multiplication of $S_D^2$ we obtain the equation

$$\zeta \int_{\Gamma_D} p\, n_z d\Gamma_D - Bl\left(Z_{MD} + S_D^2 Z_{AB}\right) u_D = 0, \tag{12}$$

where $\zeta = 4$ arises due to the quarter symmetry. Additionally, the LPM velocity is coupled to the BEM by assuming continuity of the velocity so that

$$\mathbf{c}_u u_D = \mathbf{u}_{z,D} \quad \text{on} \quad \Gamma_D, \tag{13}$$

where $\mathbf{u}_{z,D}$ is the z-component of the BEM velocity on $\Gamma_D$ and $\mathbf{c}_u$ is a vector of ones with the size of $\mathbf{u}_{z,D}$. For boundaries not on $\Gamma_D$, the surface is considered rigid, so

$$u_n = 0 \quad \text{on} \quad \Gamma \setminus \Gamma_D. \tag{14}$$

Hereafter, the BEM can be extended to include the LPM by solving the system of equations given by

$$\begin{bmatrix} \mathbf{A} & i\omega\rho\mathbf{B}_D & \mathbf{0} & \mathbf{0} \\ \mathbf{0} & \mathbf{C}_p & \mathbf{0} & -\mathbf{c}_u \\ \mathbf{0} & \mathbf{0} & Z_E & Bl \\ \zeta\mathbf{s}_n & \mathbf{0} & -Bl & \left(Z_{MD} + S_D^2 Z_{AB}\right) \end{bmatrix} \begin{bmatrix} \mathbf{p} \\ \mathbf{u}_{z,D} \\ i_c \\ u_D \end{bmatrix} = \begin{bmatrix} \mathbf{0} \\ \mathbf{0} \\ V_0 \\ 0 \end{bmatrix}, \tag{15}$$

where $\mathbf{B}_D$ is the matrix created from collocation of the single layer potential evaluated on $\Gamma_D$, the surface of the diaphragm, using the boundary condition assuming piston motion of the diaphragm (assuming zero velocity elsewhere). Hence, the single layer potential becomes,

$$\begin{aligned} &\int_{\Gamma_D} G_s \frac{\partial p(Q)}{\partial n} d\Gamma(Q) = \\ &- i\omega\rho \int_{\Gamma_D} G_s \mathbf{n}_z(Q) \cdot \mathbf{u}_{z,D}(Q) d\Gamma(Q), \end{aligned} \tag{16}$$

with $\mathbf{n}_z$ being a vector with the z-components of the normals on $\Gamma_D$. Moreover, in Eq. (15) $C_p$ is a coupling term containing ones at the corresponding coupling nodes, $i_c$ is the electrical current in the voice coil, $V_0$ is the driving voltage, $Bl$ is the force factor and $S_D$ is the effective surface area of the diaphragm. The pressure coupling vector $\mathbf{s}_n$ is obtained from discretization of

$$\mathbf{s}_n = \int_{\Gamma_D} \mathbf{N} \cdot \mathbf{n}_z \mathrm{d}\Gamma_D, \tag{17}$$

where $\mathbf{N}$ are the shape functions. The system in Eq. (15) will in the following be referred to in the compact form

$$\mathbf{A}_k \mathbf{x}_k = \mathbf{f}, \tag{18}$$

where $k$ indicates the $k$-th frequency at which the system is solved for. The system of equations is solved using the iterative generalized minimal residual (GMRES) solver found in MATLAB.

## 4 Quarter symmetric spherical loudspeaker test case

The initial geometry of the loudspeaker used as a test case for the shape optimization is depicted in Figure 2. The geometry consists of a spherical loudspeaker cabinet with a moving coil loudspeaker mounted on the sphere pointing in the z-direction. The spherical cabinet can be considered one of the better design choices for a loudspeaker cabinet since it reduces the effect of e.g. edge diffraction and therefore is a good candidate as an initial starting guess for the shape optimization (Olson, 1951). To further reduce the computational complexity, the numerical problem is formulated assuming quarter symmetry. Figure 2 also depicts the quarter-symmetric part of the geometry that is used for the numerical simulation and the associated BEM mesh. The mesh is created using six noded triangular isoparametric quadratic boundary elements with the initial mesh having six elements per wavelength assuming an upper frequency of 12 kHz. This equates to a mesh with 9542 nodes and 4770 elements. The shape optimization will only be carried out with optimization frequencies between 1 and 5 kHz. However, during the optimization the mesh will be distorted and hence an initial dense mesh is required. Alternatively, a re-meshing approach could be adopted to adjust the mesh density to reflect the current design shape or optimization frequency. The presented optimization approach uses the same mesh for all design iterations and optimization frequencies for simplicity. The radius of the initial spherical cabinet and loudspeaker unit is $R_{cab} = 8.2$ cm and $R_{unit} = 2.02$ cm, respectively. A sketch of the loudspeaker including the dimensions and the boundary conditions is shown in Figure 3. In the sketch, the entire boundary is given by $\Gamma = \Gamma_D + \Gamma_C$ with $\Gamma_C$ being the remaining surface excluding the diaphragm. The LPM of the loudspeaker is modelled using the electrical, mechanical and acoustic lumped element values as given in Tables 1, 2 and 3, respectively. The values are obtained from Klippel GmbH measurements of a non-commercial 2" full-range driver.

Table 1: Electrical parameters used in the LPM

| $V_0$ | $R_E$ | $L_E(\omega)$ | $Bl$ |
|---|---|---|---|
| $\sqrt{2}$ | 3.7 | $(i\omega)^{0.8} \cdot 0.09 \cdot 10^{-3}$ | 3.33 |

Table 2: Mechanical parameters used in the LPM

| $M_{MD}$ | $R_{MS}$ | $C_{MS}$ | $S_D$ |
|---|---|---|---|
| $2.31 \cdot 10^{-3}$ | 0.17 | $0.73 \cdot 10^{-3}$ | $1.28 \cdot 10^{-3}$ |

Table 3: Acoustic parameters used in the LPM.

| $C_{AB}$ | $R_{AB}$ | $M_{AB}$ |
|---|---|---|
| $2.04 \cdot 10^{-8}$ | 200 | $2.47 \cdot 10^{3}$ |

## 5 Parametrization using Free Form Deformation

FFD is a method to map a disctretized geometry to an underlying set of basis functions, e.g, Bernstein polynomials, B-splines etc. Traditional FFD will typically use a Cartesian grid from which the geometry can be de-

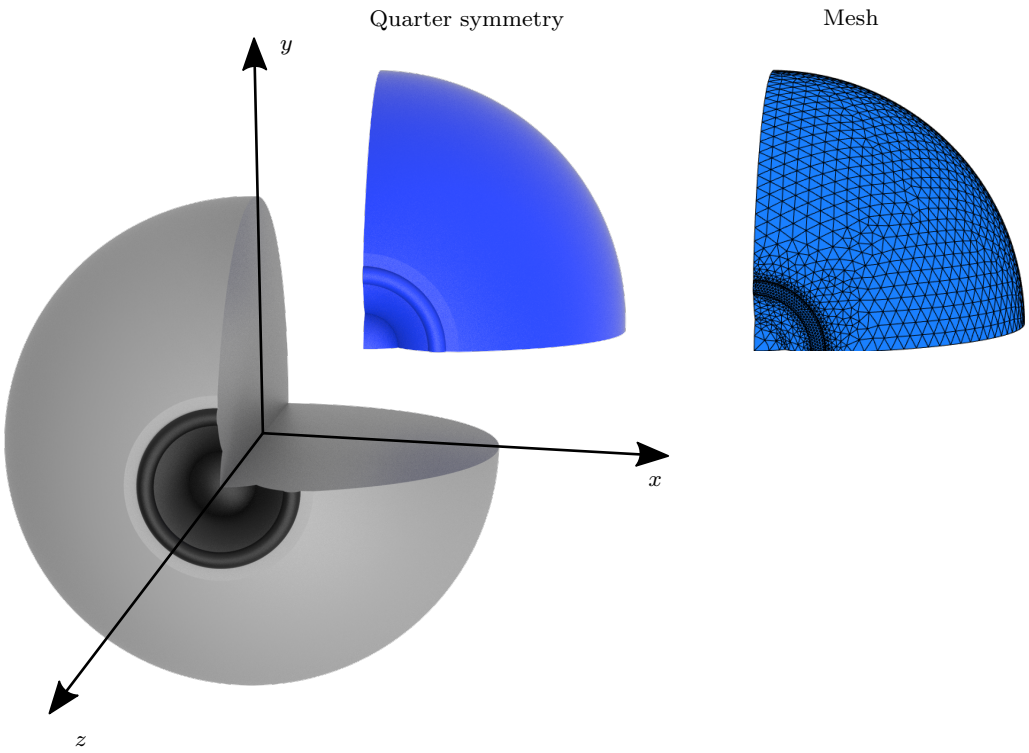


Fig. 2: The spherical loudspeaker geometry. The Figure includes both the part of the geometry that is modelled assuming symmetry and the associated boundary mesh.

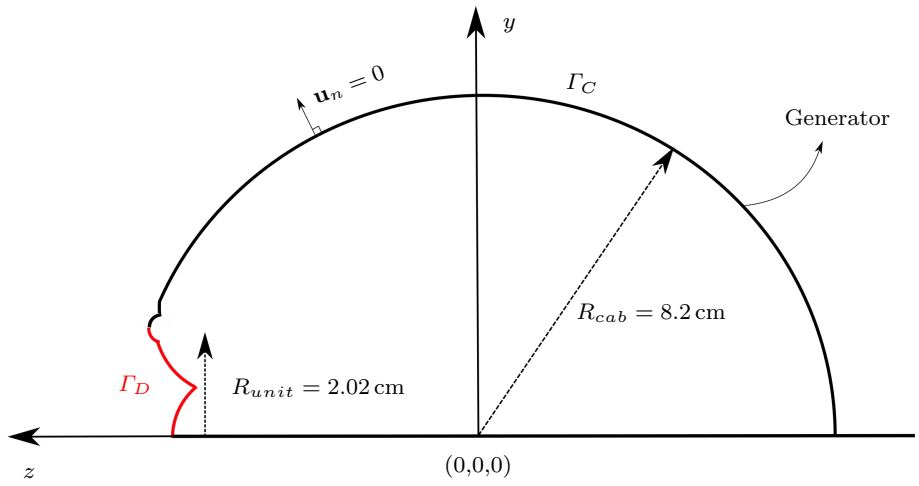


Fig. 3: A sketch of the loudspeaker system including the dimensions and the location of the boundary conditions used in Eq. (15).

scribed (Sederberg, 1986). However, in the case of the spherical loudspeaker cabinet it is beneficial to develop the parametrization region using a more suitable coordinate system. In the case of the presented loudspeaker it is natural to use a spherical coordinate system to describe the FFD region. Using a spherical coordinate system and Bernstein polynomials as basis functions, the nodal coordinates in the FFD region can be expressed as

$$\begin{bmatrix} r(s) \\ \theta(t) \\ \phi(u) \end{bmatrix} = \sum_{i=0}^{l}\sum_{j=0}^{m}\sum_{k=0}^{n} B_{i,l}(s)B_{j,m}(t)B_{k,n}(u) \begin{bmatrix} r_{i,j,k} \\ \theta_{i,j,k} \\ \phi_{i,j,k} \end{bmatrix}, \tag{19}$$

where $0 < s < 1$, $0 < t < 1$ and $0 < u < 1$ is the local parameter space of the FFD region.The Bernstein polynomial that depends on $s$ is given by

$$B_{i,l}(s) = \binom{l}{i} s^i (1-s)^{l-i}. \tag{20}$$

Similarly, $B_{j,m}(t)$ and $B_{k,n}(u)$ can be obtain from the same function as in Eq. (20), but with different notation. The corresponding Cartesian coordinates can be found as

$$x(s,t,u) = r(s)\cos(\theta(t))\sin(\phi(u)) + x_0, \tag{21}$$
$$y(s,t,u) = r(s)\sin(\theta(t))\cos(\phi(u)) + y_0, \tag{22}$$
$$z(s,t,u) = r(s)\cos(\phi(u)) + z_0, \tag{23}$$

where $x_0$, $y_0$ and $z_0$ is used as an offset to control the location of the spherical FFD region. Nodal coordinates of the mesh inside the non-deformed FFD region can be mapped to the local $s$, $t$ and $u$ coordinates by using the linear maps

$$s = \frac{r_p - r_{\max}}{r_{\max} - r_{\min}}, \quad t = \frac{\theta_p - \theta_{\max}}{\theta_{\max} - \theta_{\min}}, \quad u = \frac{\phi_p - \phi_{\max}}{\phi_{\max} - \phi_{\min}}, \tag{24}$$

where $r_p$, $\theta_p$ and $\phi_p$ are the spherical coordinate representation of the computational nodes inside the FFD region. The subscripts *min* and *max* denote the size of the different parameters in the initial FFD region. An example of the spherical FFD region with the control points is depicted in Figure 4.

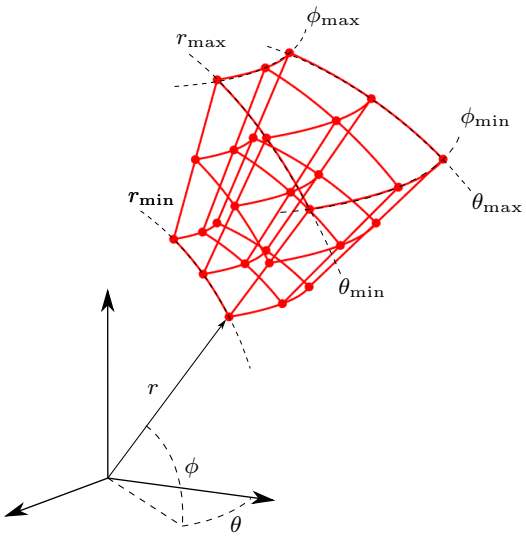


Fig. 4: Example of a spherical FFD region with $m = n = l = 2$. Red dots represent control points.

### 5.1 Parametrization of the spherical loudspeaker mesh and linking of control points

Figure 5a shows the spherical FFD parametrization that is used to control the shape of the spherical loudspeaker cabinet. The red dots denote the control points given from the spherical coordinates $r_{i,j,k}$, $\theta_{i,j,k}$ and $\phi_{i,j,k}$. The initial size of the FFD region is defined by the limits $r_{\min}$, $r_{\max}$, $\theta_{\min}$, $\theta_{\max}$, $\phi_{\min}$ and $\phi_{\max}$. The FFD parametrization is based on the initial parameters given by: $r_{min} = 7\,\text{cm}$, $r_{max} = 8.3\,\text{cm}$, $\theta_{\min} = 0\,\text{rad}$, $\theta_{\max} = \frac{\pi}{2}\,\text{rad}$, $\phi_{\min} = -\frac{\pi}{2}\,\text{rad}$, $\phi_{\max} = 1.227\,\text{rad}$, $l = 1$, $m = 8$ and $n = 16$. Here, $\phi_{\max} = 1.227$ is used to avoid the parameterization to overlap the loudspeaker unit (see Figure 5). Also, the parameters $r_{min}$ and $r_{max}$ are chosen so the spherical geometry lies with-in the FFD region. In principle it would be possible to create a parametrization that only consists of a single layer of control points in the radial direction. However, having a volumetric description of the parametrization makes the description general and applicable in situations where the underlying mesh is necessarily not spherical, although this is outside the scope of the present work. In general, the parametrization will only enforce $C^0$ continuity of the computational nodes located on the symmetry planes. Therefore, the optimization is very likely to create sharp edges at the symmetry planes. This can potentially create numerical errors, extraordinarily large field variables and large sensitivity to small design changes close to such sharp edges. This behaviour is to a degree circumvented by linking together the two control points closest to the symmetry plane together into one single design variable. An ex-

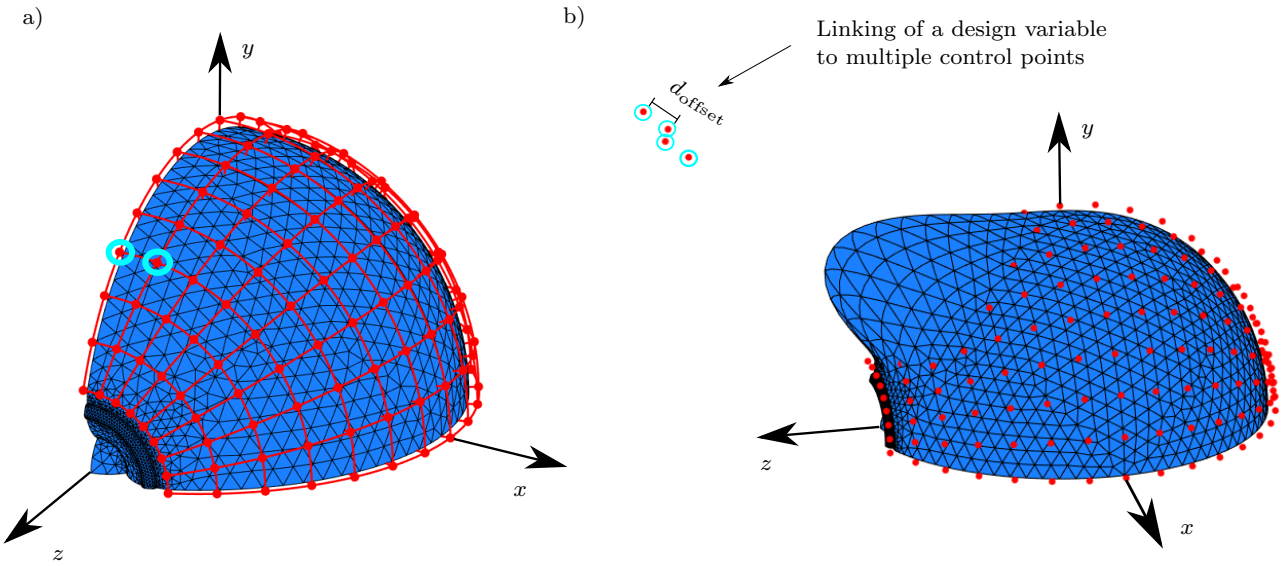


Fig. 5: The FFD parametrization used to describe the geometry of the loudspeaker cabinet with the red dots representing the control points. In figure a), the initial spherical FFD parametrization is shown. The initial parametization is based on the following spherical FFD parameters: $r_{min} = 7\,\text{cm}$, $r_{max} = 8.3\,\text{cm}$, $\theta_{\min} = 0\,\text{rad}$, $\theta_{\max} = \frac{\pi}{2}\,\text{rad}$, $\phi_{\min} = -\frac{\pi}{2}\,\text{rad}$, $\phi_{\max} = 1.227\,\text{rad}$, $l = 1$, $m = 8$ and $n = 16$. Figure b) shows the perturbation of a single design variable, and how a single design variable is linked to multiple control points along the r-direction and the two control points closest to the symmetry plane. The control points linked together are marked with cyan colored circles.

ample of the two control points closest to the symmetry plane is marked with cyan circles in Figure 5a. Furthermore, to reduce the number of design variables, only movement in the radial direction is used as design variables. Therefore, also control points in the same radial direction are linked into a single design variable with a constant offset $d_{\text{offset}} = r_{\max} - r_{\min}$, given by the initial location of the control points. The control point linking and an example of the perturbation of a single design variable at the symmetry axis are depicted in Figure 5b. This means that close to a the symmetry plane a design variable will change the location of four control points and in all other places a design variable consists of two control points. The design variables are collected into the vector $\mathbf{v}$ where the $l$-th entry in $\mathbf{v}$ is given by $v_l$ which are scaled so that $0 \leq v_l \leq 1$ using

$$v_l = \frac{r_{i,j,k} - L_l}{L_u - L_l}, \tag{25}$$

where $L_u$ and $L_l$ are the upper and lower optimization bounds on the the radial control point $r_{i,j,k}$, respectively. In the shape optimization studies $L_l = 7.3\,\text{cm}$ and $L_u = 22.3\,\text{cm}$. The optimization bounds are chosen so the cabinet size is not too small and so that the mesh quality remains reasonable in the case of large deformations. Note that the upper and lower optimization bounds are different from $r_{min}$ and $r_{max}$ which are parameters used to construct and specify the size of the initial FFD region.

## 6 Optimization problem formulation

The objective of the optimization is to create a loudspeaker that is less directive in the frequency range between 1 kHz to 5kHz. However, this statement does not have a single obvious mathematical description. The goal could be formulated as having a SPL that is independent of frequency and orientation within a predefined spatial region and frequency range. In its raw form, this would lead to an optimization problem with as many constraints as there are frequency times directivity measurement points. Due to the cost of evaluating the sensitivities for such large scale problems, later in this section we will propose and numerically investigate two formulations aimed at reducing the computational cost while still reasonably meeting the optimization goals. These formulations are based on assuming the validity of a representation of the directivity as the root mean square deviation (RMSD) of the SPL at several locations in front of the loudspeaker using the

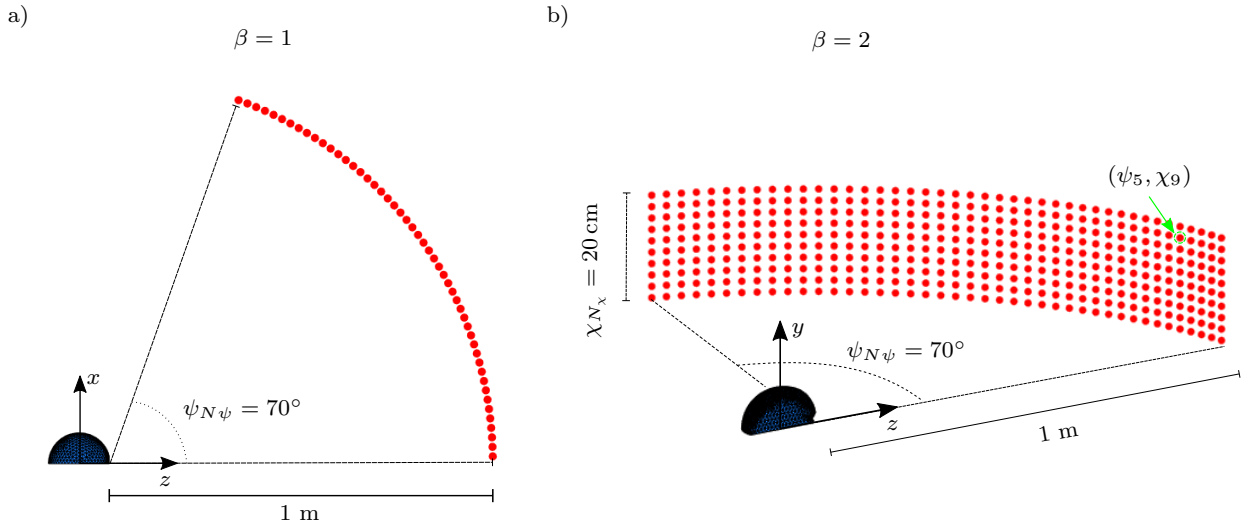


Fig. 6: The distribution of field points $(\psi_i, \chi_j)$ used to evaluate the cost function defined in Eq. (26). In figure a), the field points are only defined in the xz-plane and in b) extra field points are added in the y-direction. Figures a) and b) represent the optimziation problem with $\beta = 1$ and $\beta = 2$, respectively.

following expression

$$\phi_k(\mathbf{v}) = \sqrt{\frac{1}{N_\psi N_\chi} \sum_{j=1}^{N_\chi} \sum_{i=1}^{N_\psi} \left(\mathrm{SPL}(\psi_i, \chi_j, \mathbf{v}) - \mu(\mathbf{v})\right)^2}, \tag{26}$$

where $\phi_k(\mathbf{v})$ is the cost function evaluated at the $k$-th frequency using the design variables contained in the vector $\mathbf{v}$. Moreover, $\mathrm{SPL}(\psi_i, \chi_j, \mathbf{v})$ is the Sound Pressure Level at the location $(\psi_i, \chi_j)$ where $\psi_i$ is a azimuth angle in front of the loudspeaker and $\chi_j$ is a y-coordinate (see e.g. Figure 6 ), $N_\psi$ is the number of field points in the azimuthal direction, $N_\chi$ is the number of field points in the y-direction and $\mu$ is the average SPL of all the different field points, given by

$$\mu(\mathbf{v}) = \frac{1}{N_\psi N_\chi} \sum_{j=1}^{N_\chi} \sum_{i=1}^{N_\psi} \mathrm{SPL}(\psi_i, \chi_j, \mathbf{v}). \tag{27}$$

where the SPL, assuming harmonic excitation, is defined as (Kinsler, 2000)

$$\mathrm{SPL}(\psi_i, \chi_j, \mathbf{v}) = 20\log_{10}\left(\frac{\frac{1}{\sqrt{2}}|p(\psi_i, \chi_j, \mathbf{v})|}{p_{ref}}\right) \tag{28}$$

with $p_{ref}$ equal to 20 $\mu$Pa and $p(\psi_i, \chi_j, \mathbf{v})$ being a field point obtained from Eq. (3). The field point pressure used to evaluate the SPL depends on the design variables $\mathbf{v}$ though the computational domain $\Omega$ appearing in Eq. (1). The field points where the cost function is evaluated are located 1 m away from the loudspeaker system with the top of the loudspeaker dust cap being considered the acoustic center. Two different configurations are used to distribute the field points. In the first case, the field points are located in the xz-plane (along an azimuth angle $\psi$) as sketched in Figure 6a. In the second case field points are distributed in the same way as in Figure 6a, but also with field points distributed along the y-direction as sketched in Figure 6b.

Based on this initial description of the spatial variation of the SPL, the optimization problem will be investigated using two different optimization approaches, both concerning the frequency dependence. In the first case, the optimization problem is described using a weighted average of $\phi_k$ evaluated at the optimization frequencies. Hence, the optimization problem can formally be stated as

$$\begin{aligned} \min_{\mathbf{v}} \quad & \phi_{A,\beta}(\mathbf{v}) = \tfrac{1}{N_k} \textstyle\sum_{k=1}^{N_k} w_k \phi_k(\mathbf{v}), \\ \text{s.t.} \quad & \mathbf{A}_k \mathbf{x}_k - \mathbf{f} = 0\,, && k = 1, \ldots, N_k \\ & 0 \leq \ v_l \leq 1\,, && l = 1, \ldots, n. \end{aligned} \tag{29}$$

It is noted that $\mathbf{A}_k \mathbf{x}_k - \mathbf{f} = 0$ (the system equation in Eq. (18)) is included as an unconstrained problem in its nested form. Moreover, $N_k$ is the number of frequencies included in the optimization and $w_k$ is the weighting of the cost function at the individual optimization frequencies. Furthermore, the subscript $A$ indicates that $\phi_k$ is evaluated as the weighted average and the subscript $\beta$ is either 1 or 2 depending on whether the cost function is evaluated at the field points in Figure

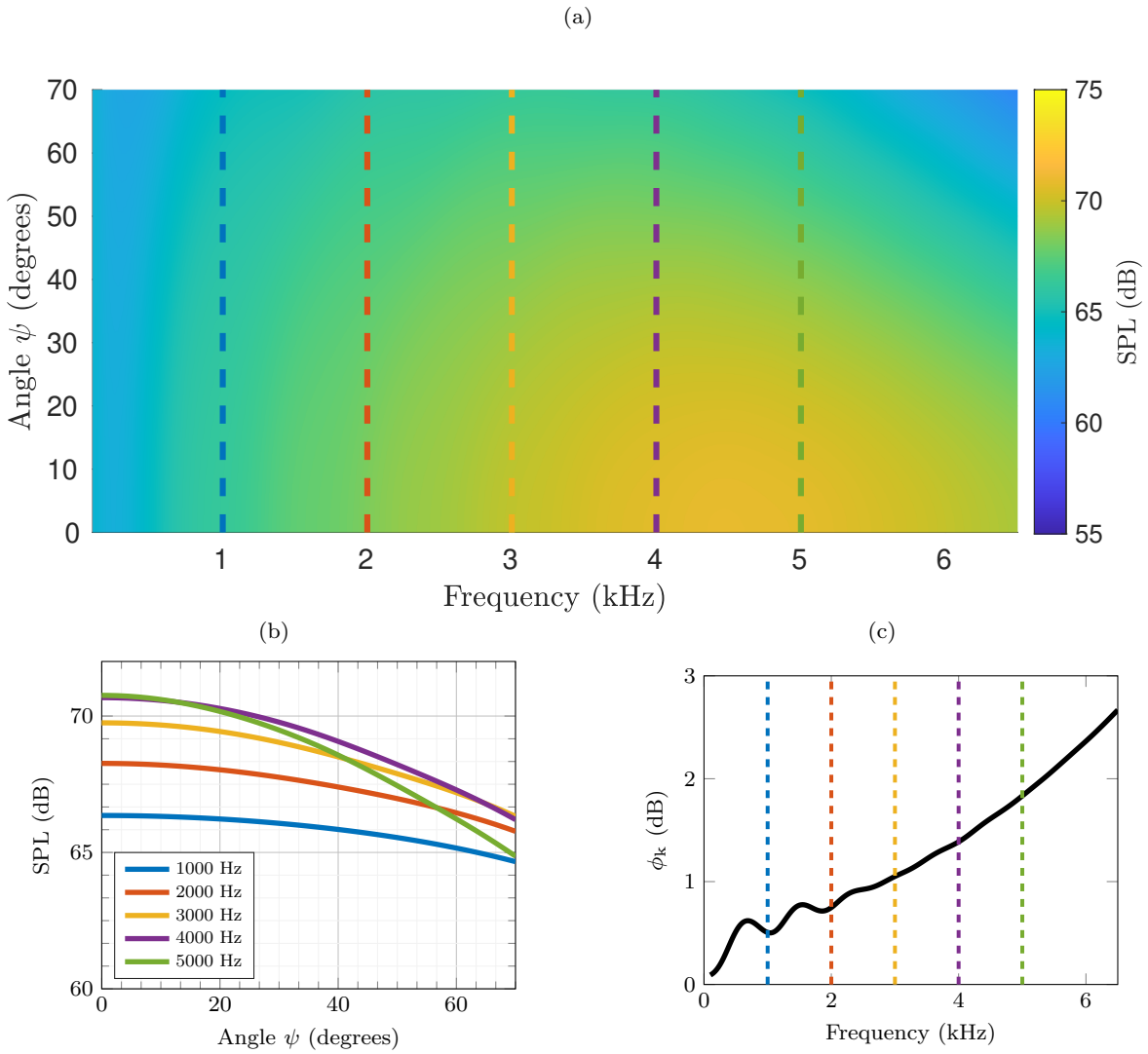


Fig. 7: The performance of the initial spherical loudspeaker using the field point distribution as depicted in Figure 6a. In the figure, a) is the SPL directivity as a function of frequency and the angle $\psi$, b) is the SPL along the field points seen in Figure 6a for the five optimization frequencies, and c) is the cost function $\phi_k$ as a function of frequency evaluated from 100 Hz to 6.5 kHz. The vertical colored dashed lines represent the location of the optimization frequencies.

6a or Figure 6b, respectively. The optimization problem in Eq. (29) is solved using the sequential quadratic programming (SQP) implementation in the MATLAB function *fmincon*.

The second optimization approach is a minimax formulation where the largest value of $\phi_k$ is minimized, i.e. the optimization frequency with the maximum value of the cost function is minimized. The minimax optimization problem is formulated as

$$\begin{aligned} \min_{\mathbf{v}} \max_{k} \; & \phi_{B,\beta}(\mathbf{v}) = \phi_k(\mathbf{v}) \;, \; k = 1, \ldots, N_k \\ \text{s.t.} \quad & \mathbf{A}_k \mathbf{x}_k - \mathbf{f} = 0 \;, \quad k = 1, \ldots, N_k \\ & 0 \leq \; v_l \leq 1 \;, \quad l = 1, \ldots, n. \end{aligned} \tag{30}$$

The minimax problem is solved as a bound formulation using the *fminimax* function in MATLAB. It should also be noted that during the optimization the cost function and the sensitivities are scaled with the initial solution.

Finally, we remark that we do not include a volume constraint in any of the presented optimization problem

formulations. Although optimized designs of smaller volume is clearly desired from a practical perspective, our numerical experiments have shown we are able to implicitly control the final volume based on the size of the initial configuration (see section 8.6 for details).

## 7 Discrete semi-analytical adjoint sensitivites

The design sensitivities are calculated using a discrete adjoint approach, i.e., the matrix derivatives are evaluated semi-analytically using finite difference. The design sensitivities for time-harmonic acoustic problems are found as (Jensen and Sigmund, 2005; Dühring et al., 2008)

$$\frac{\mathrm{d}\phi_k}{\mathrm{d}v_l} = \frac{\partial \phi_k}{\partial v_l} + \Re\left(\boldsymbol{\lambda}^{\mathrm{T}}\left(\frac{\partial \mathbf{A}_k}{\partial v_l}\mathbf{x}_k\right)\right), \tag{31}$$

where $\boldsymbol{\lambda}$ is a vector containing the Lagrange multipliers and $\Re$ is the real part operator. The Lagrange multipliers are found by solving the adjoint problem

$$\mathbf{A}_k^{\mathrm{T}}\boldsymbol{\lambda} = -\left(\frac{\partial \phi_k}{\partial \mathbf{x}_{k,r}} - \mathrm{i}\frac{\partial \phi_k}{\partial \mathbf{x}_{k,i}}\right)^{\mathrm{T}}, \tag{32}$$

where the subscripts $r$ and $i$ denote the real and imaginary part of the state vector $\mathbf{x}$, respectively. To improve the performance of the matrix derivative calculations, a reduced assembly approach is applied (Andersen et al., 2020, 2021). This approach is mainly beneficial if the parametrization covers a small portion of the geometry or if the parametrization has compact support. This is not the case in the parametrization presented here. Nevertheless, the adjoint method still offers a significant speed-up and accuracy. As it is with a finite difference, the step-length can influence the accuracy of the sensitivities. To further elaborate on the choice of steplength in the matrix derivatives a small study is carried out in Appendix B. Alternatively, there are examples in the literature of analytical design sensitivities being developed based on the continuous BEM equations (Matsumoto et al., 2011). Analytical sensitivities have the benefit of potentially being more accurate. However, they are more cumbersome to implement and their description needs to be adapted depending on the underlying parameterization.

## 8 Results

The results of the shape optimization are presented in the following. All optimization studies are carried out using five equally spaced optimization frequencies between 1 and 5 kHz. Alternatively, logarithmic spacing could be used for a more perceptual measure. However, a linear spacing is chosen to have more emphasis on the higher frequencies where the acoustic problem is expected to be more sensitive to design changes. The optimization examples are either run until Karush-Kuhn-Tucker (KKT) conditions meet the default tolerance or to a maximum of 80 iterations, which have been proven sufficient to only have a very small change in the cost function between the last iterations. In total, the FFD parametrization consists of 98 design variables utilizing the control point linking approach previously described. The optimization time ranges between four to six days depending on whether the optimization is performed with *fmincon* or *fminimax*, with a parametrization consisting of 98 design variables. In general, the SQP algorithm in *fmincon* has been faster as compared to the minimax implementation. The hardware used to solve the shape optimization problems is a workstation equipped with an 18 core Intel Xeon W-2295 and 256 GB of memory.

### 8.1 The performance of the initial design

To compare the optimization performance, the SPL directivity response from 0 to 70 degrees of the initial design is plotted in Figure 7a (calculated using the field point distribution given in Figure 6a). The plots show, as expected, how the loudspeaker becomes more directive for higher frequencies. Additionally, Figure 7b includes the SPL distribution at the individual optimization frequencies. Furthermore, Figure 7c plots the cost function $\phi_k$ as a function of frequency using the field point distribution in Figure 6a ($\beta = 1$), displaying how the loudspeaker directivity increases with frequency.

### 8.2 Shape optimization of the spherical loudspeaker using frequency weighting

The first shape optimization example uses $\phi_{A,1}$ as the cost function. Optimization using $\phi_{A,1}$ requires a definition of the weighting function. In the following, two different weighting approaches are investigated. In the first case, each optimization frequency has equal weighting, so that

$$w_k = 1 \,\forall\, k. \tag{33}$$

In the second case, a logarithmic frequency dependent weighting is used, where

$$w_k = w_{\mathrm{fd}} = \left(\log_{10}\left(\frac{f_k}{f_{\min}}\right) + 1\right)^{-1}, \tag{34}$$

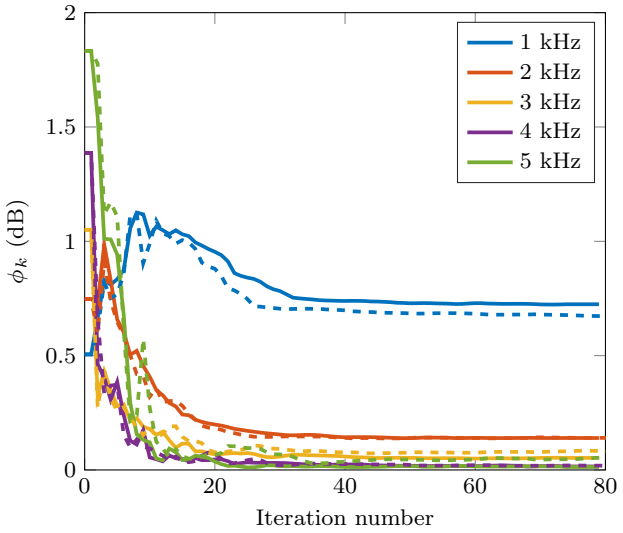


Fig. 8: The evolution of the cost function $\phi_k$ using optimization with the two different weighting approaches defined in Eqs. (33) and (34). Solid and dashed lines correspond to optimization with equal and frequency dependent weighting, respectively.

with $f_k$ being the current optimization frequency and $f_{\text{min}}$ the lowest optimization frequency. This scaling is chosen due to the following reasoning. In general, it is expected that it can be more difficult to minimize $\phi_k$ for higher frequencies. At higher frequencies, it is well-known that the loudspeaker will start to become more directive as the wavelength becomes comparable with the size of the loudspeaker unit (Kinsler, 2000, p. 179). A behavior that potentially can be hard to circumvent from just changing the cabinet shape. Therefore, an example is included where higher frequencies have a lower weighting and hence are less important seen from the point of view of the optimizer. It can be seen as an attempt to distribute optimization effort proportionally to the physical difficulty of reducing the directivity.

In Figure 8, the evolution of the cost functions using the two different weighting approaches to describe $\phi_{A,1}$ is shown. As is observed, the two optimization cases converge to very similar performance when comparing the cost functions. Here, the cost functions for the two weighting approaches are evaluated without any weighting to make the evolution more comparable. Solid lines correspond to optimization with equal weighting and dashed lines are the optimization with frequency dependent weighting. As it is expected, the optimization performed with the frequency dependent weighting has the lowest value for the lowest optimization frequency if compared to the optimization carried out with equal weighting. Inspecting the two optimized designs shown in Figures 9 and 10, it is seen that the two designs show very similar design features. A common feature is e.g. the extension of the shape directly above the loudspeaker in the y-direction. The colormaps in the two figures are the difference $R_d = \|\mathbf{x}_{\text{in}} - \mathbf{x}_{\text{op}}\|$ between the computational nodes in of the optimized design, $\mathbf{x}_{\text{op}}$, and the initial mesh, $\mathbf{x}_{\text{in}}$.

The performances of the two shape optimization designs are evaluated in Figures 11 and 12. Inspecting the directivity plots (Figure 11a and 12a), the behaviour and performance of the two designs are very similar. In general, for the two optimized designs, the performance is better at the higher optimization frequencies. This is e.g reflected in both Figures 11c and 12c, where the cost function $\phi_k$ is very close to zero at 3, 4 and 5 kHz. Even though the optimization is performed at only 5 discrete frequencies and only considering a single starting guess, the performance of the cost function $\phi_k$ for the two shape optimized designs as compared to the initial design is improved between approximately 1.5 kHz and 5 kHz. At the highest optimization frequencies, the initial difference between the on-axis SPL$(0, 0)$ and the off-axis SPL$(70, 0)$ is close to 5 dB. For the optimzed designs, this difference is close to 0 dB (see Figure 11b and 12b). Furthermore, over the frequency range 2 to 5 kHz the variation in the on-axis and off-axis is less than 1 dB. It should also be noted that the performance above 5 kHz is quickly degraded and eventually becomes even worse when compared to the initial design. Also, the performance at the optimization frequency of 1 kHz is degraded as compared to the initial design. The results contradict the expectation of the optimization being more difficult at higher frequencies. However, this is attributed to the relatively narrow region of optimization. It is expected that the optimization will become increasingly difficult for even higher frequencies. Here, the beaming effect of the loudspeaker is more pronounced and the design is more sensitive to small changes between the different optimization frequencies. A potential shortcoming of performing shape optimization with the level of design freedom given here is the risk that the underlying BEM solution becomes mesh dependent. To show this is not the case, a study is carried out in Appendix C comparing the mesh used

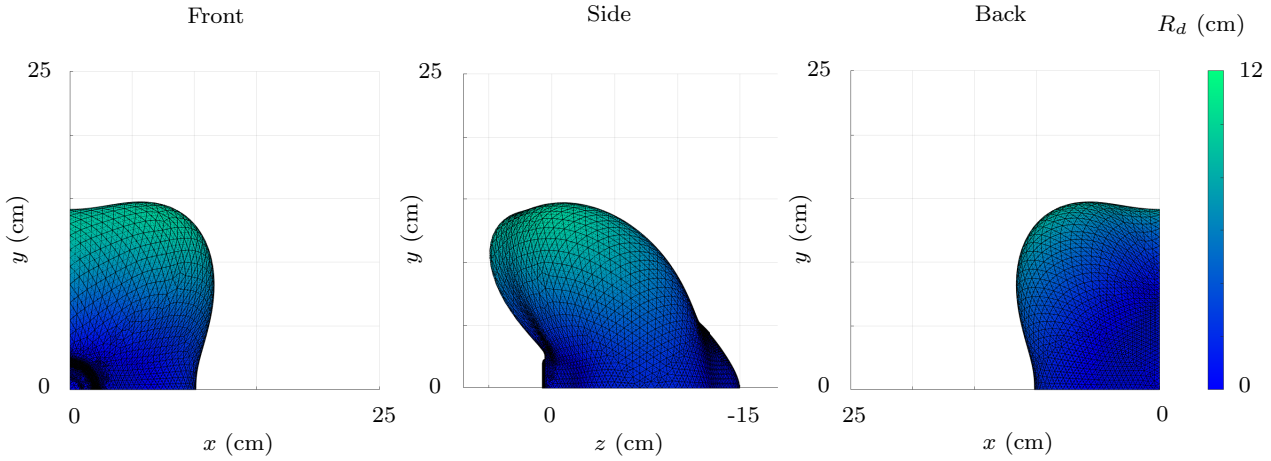


Fig. 9: The shape optimized design using $\phi_{A,1}$ with equal weighting. The colormap shows the distance between the nodes in the optimized mesh and the corresponding nodes in the initial non-pertubed mesh. A photo-realistic rendering of the geometry is shown in Figure 20a in the Appendix. Also, Figure 23a in the Appendix shows the location of the control points for the optimized design.

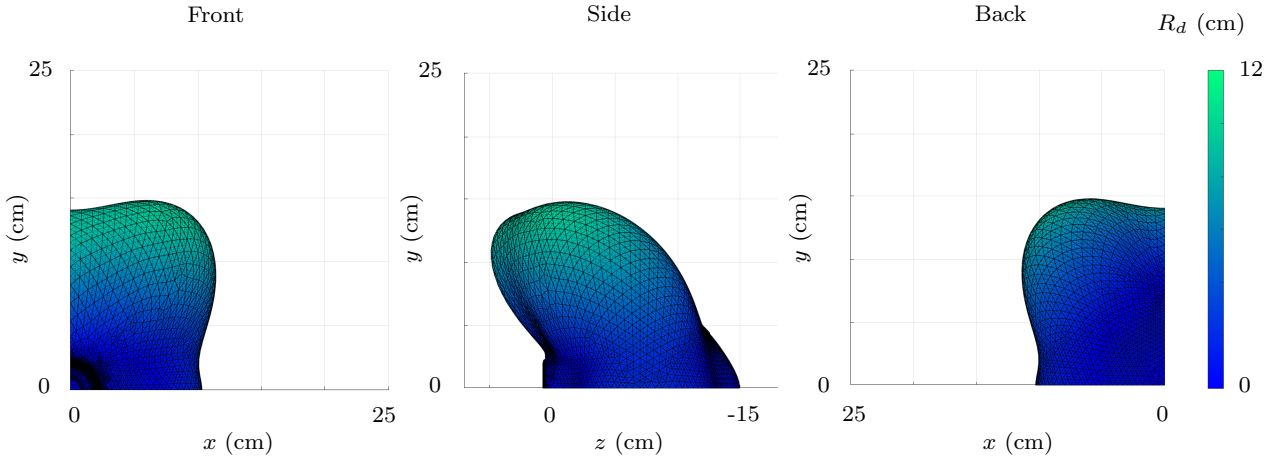


Fig. 10: The shape optimized design using $\phi_{A,1}$ with frequency dependent weighting. The colormap shows the distance between the nodes in the optimized mesh and the corresponding nodes in the initial non-pertubed mesh. A photo-realistic rendering of the geometry is shown in Figure 20b in the Appendix. Also, Figure 23b in the Appendix shows the location of the control points for the optimized design.

during optimization and a re-meshed geometry with a denser mesh of the optimized design.

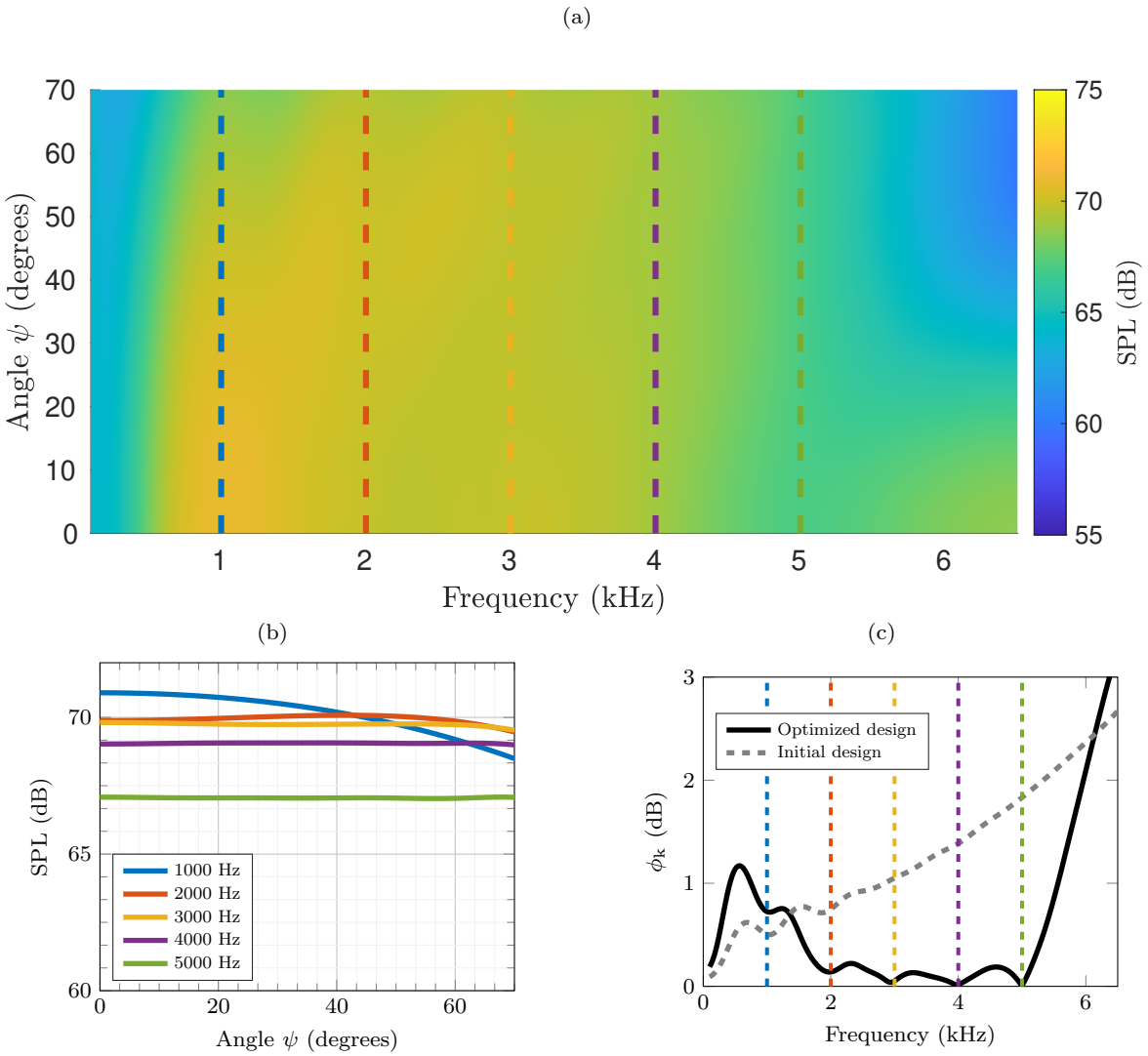


Fig. 11: The performance of the design optimized using $\phi_{A,1}$ with equal weighting . The simulations are based on the cabinet shape as seen in Figure 9. In the figure, a) is the SPL directivity of the loudspeaker evaluated in the field points as depicted in Figure 6a. The vertical colored dashed lines represent the optimization frequencies. Furthermore, b) shows the SPL along the field points seen in Figure 6a for each optimization frequency. Finally, c) is the cost function $\phi_k$ as a function of frequency for both the initial and the optimized design.

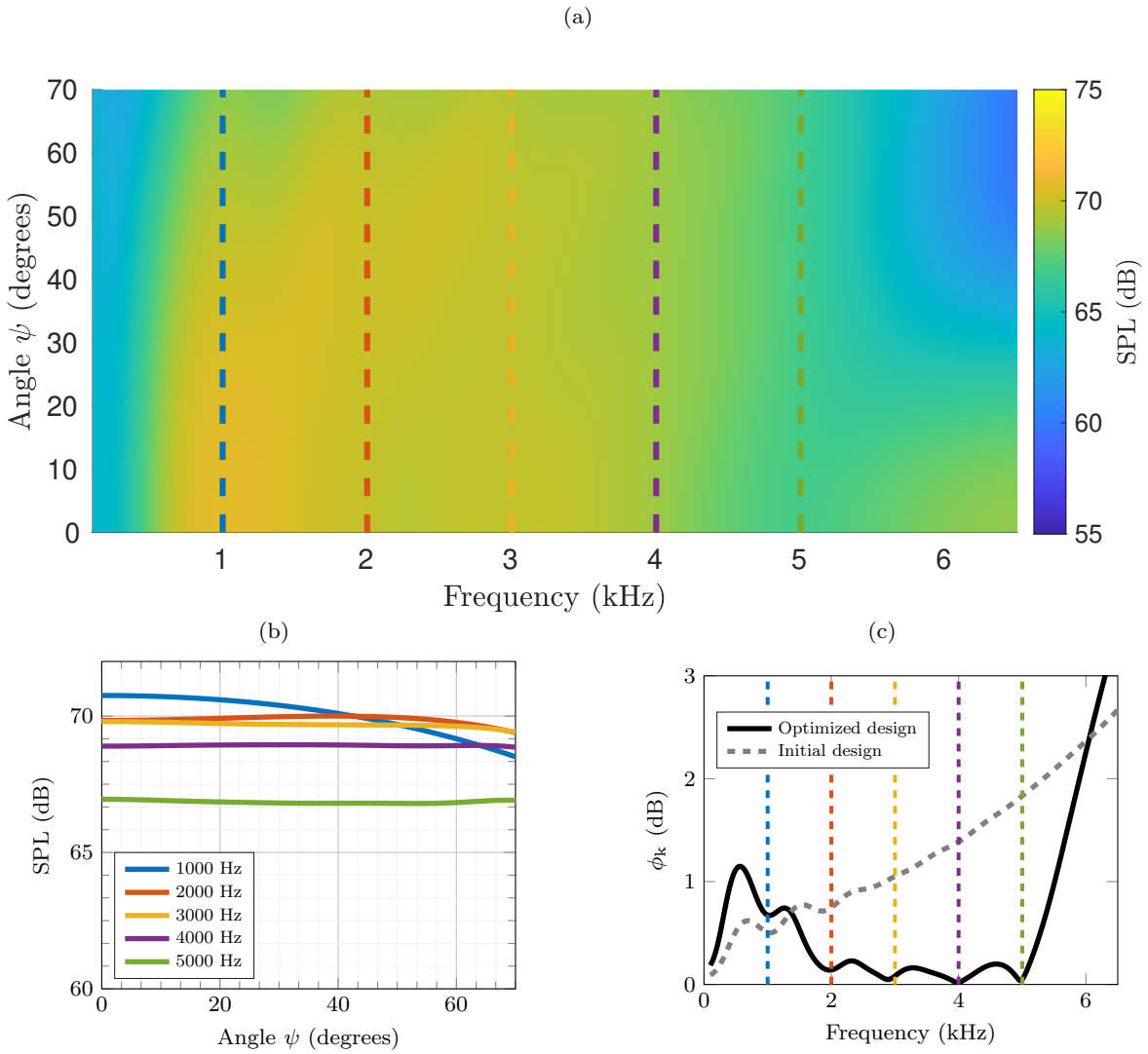


Fig. 12: The performance of the optimized design using $\phi_{A,1}$ with frequency dependent weighting. The simulations are based on the cabinet shape as seen in Figure 10. In the figure, a) is the SPL directivity of the loudspeaker evaluated in the field points as depicted in Figure 6a. The vertical colored dashed lines represent the optimization frequencies. Furthermore, b) shows the SPL along the field points seen in Figure 6a for each optimization frequency. Finally, c) is the cost function $\phi_k$ as a function of frequency for both the initial and the optimized design.

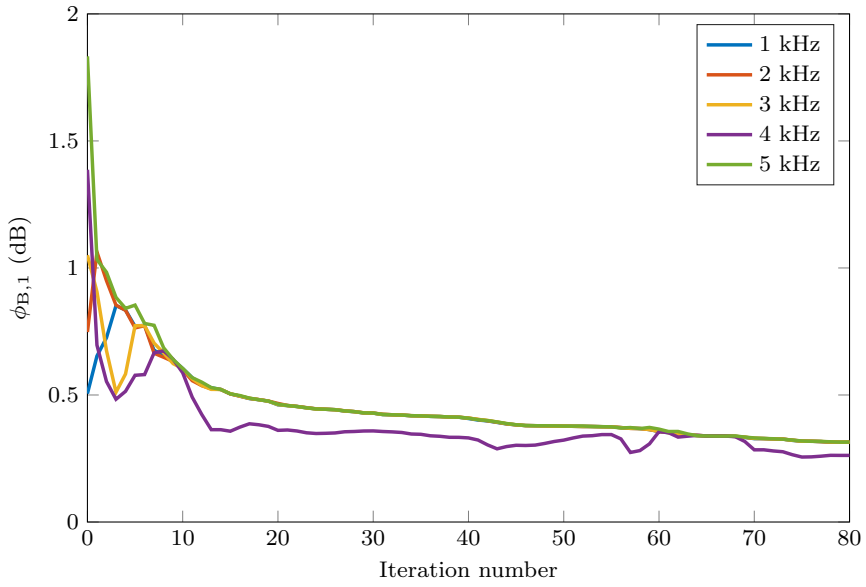


Fig. 13: The evolution of the cost functions using the minimax formulation $\phi_{B,1}$.

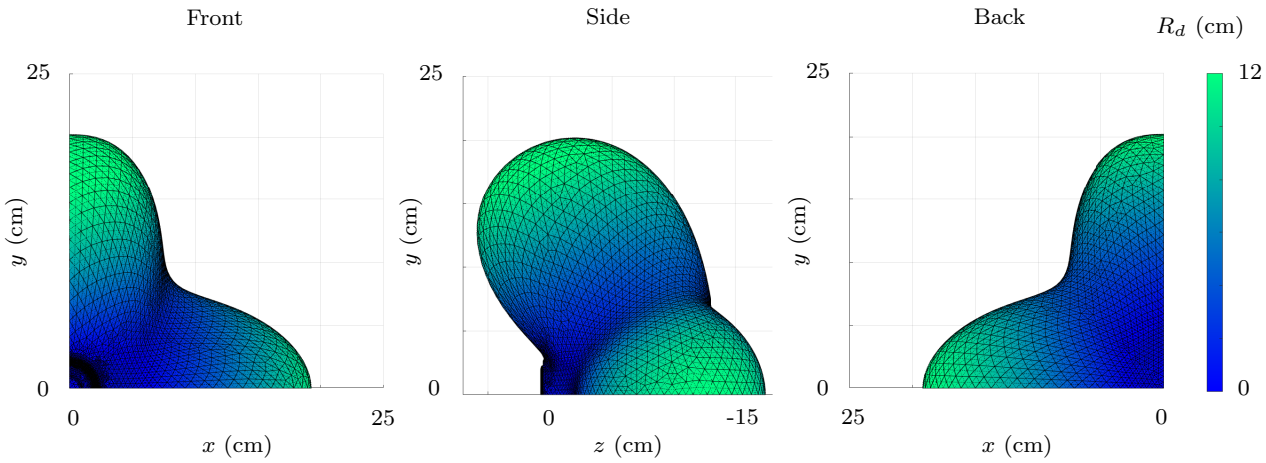


Fig. 14: The shape optimized design using the minimax problem $\phi_{B,1}$. The colormap shows the distance between the nodes in the optimized mesh and the corresponding nodes in the initial non-pertubed mesh. A photo-realistic rendering of the geometry is shown in Figure 20c in the Appendix. Also, Figure 23c in the Appendix shows the location of the control points for the optimized design.

### 8.3 Shape optimization using minimax

The next test case uses the minimax optimization formulation as defined in Eq. (30) and the field point distribution shown in Figure 6a. The evolution of the cost function for the optimization frequencies is plotted in Figure 13 and the final optimized design is shown in Figure 14. The optimized design using $\phi_{B,1}$ with the minimax formulation favors a different design choice as compared to the two previous test cases. The deformation of the design is larger and more noticeable in the x-direction. However, comparing the side view in Figures 9, 10 and 14, again a similar common feature in the design is the expansion of the geometry right above the loudspeaker in the y-direction. Similar to the previous two examples, Figure 15 shows the performance of the loudspeaker design evaluated in terms of the directivity and the cost function as a function of frequency. Inspecting Figure 15a, the directivity pattern is comparable to the two previous test cases, however, the low-frequency performance of the cost function is improved and is now better than the initial design. Also, the improvements in the cost function between 1 and 5 kHz are smaller when using the minimax formulation as compared to the summation-based cost function. This

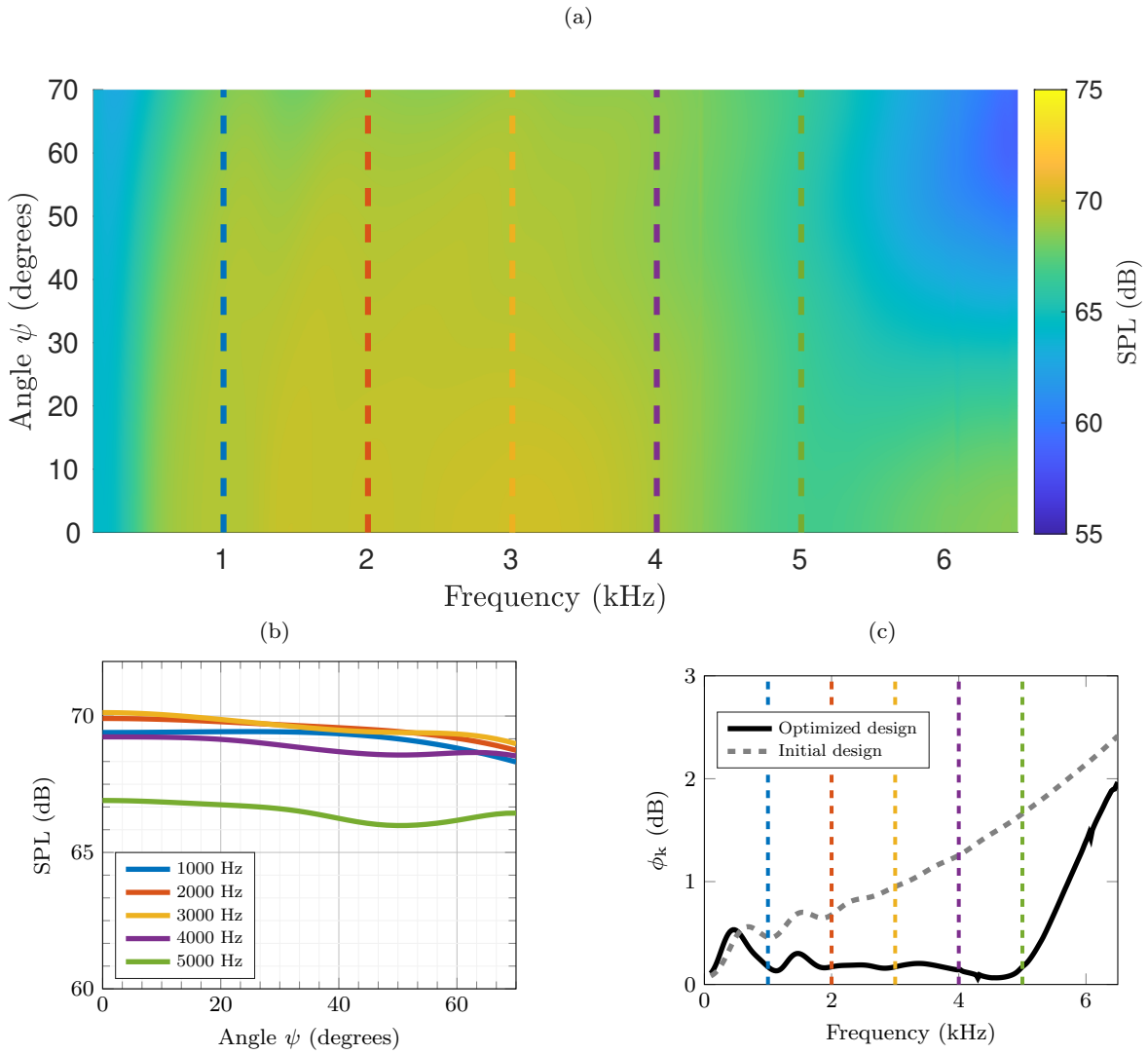


Fig. 15: The performance of the shape optimized design based on $\phi_{B,1}$. In the figure, a) is the SPL directivity, b) is the SPL at the optimization frequencies, and c) is the cost function as a function of frequency evaluated between 100 Hz to 6.5 kHz.

does however come with the sacrifice of performance at the optimization frequencies 3, 4 and 5 kHz, where the cost function does not reach values close to zero, which was the case when using the $\phi_{A,1}$. All in all, the cost function in the range from 500 Hz to around 6 kHz shows an improvement over the initial design guess and also offers a more broadband operation region with a flat directivity response.

### 8.4 Shape optimization using summation with equal weighting and minimax

To further challenge and explore the capabilities of the proposed optimization method, two additional studies are carried out using the cost function evaluation as depicted in Figure 6b ($\beta = 2$). In this case, the field points are not only located in the horizontal plane, but rather in a cylindrical surface, potentially making the minimization of the cost functions more difficult. The studies will limit themselves to using the averaged cost function with equal weights and the minimax formulation. The resulting optimized designs are shown in Figures 16 and 17, respectively. The two designs show similar behavior and features when compared to the previous designs using $\beta = 1$, e.g, common for the design presented is the change of the geometry in the y-direction above the loudspeaker unit. The optimized design obtained using $\phi_{B,2}$ shows slightly larger geometry deformations in most places as compared to the

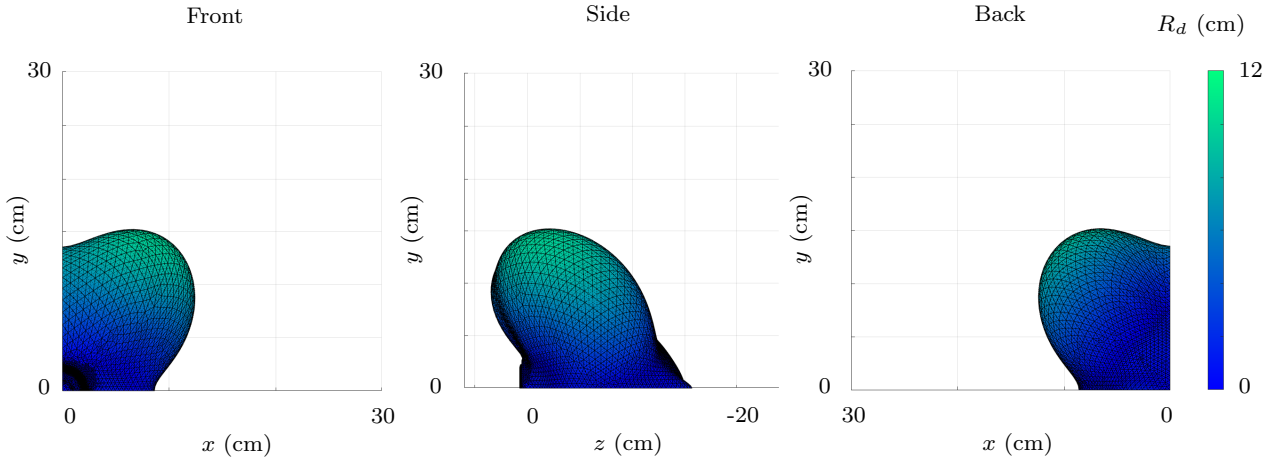


Fig. 16: The shape optimized design using $\phi_{A,2}$ with equal weighting. The colormap shows the distance between the nodes in the optimized mesh and the corresponding nodes in the initial non-pertubed mesh. A photo-realistic rendering of the geometry is shown in Figure 20d in the Appendix. Also, Figure 23d in the Appendix shows the location of the control points for the optimized design.

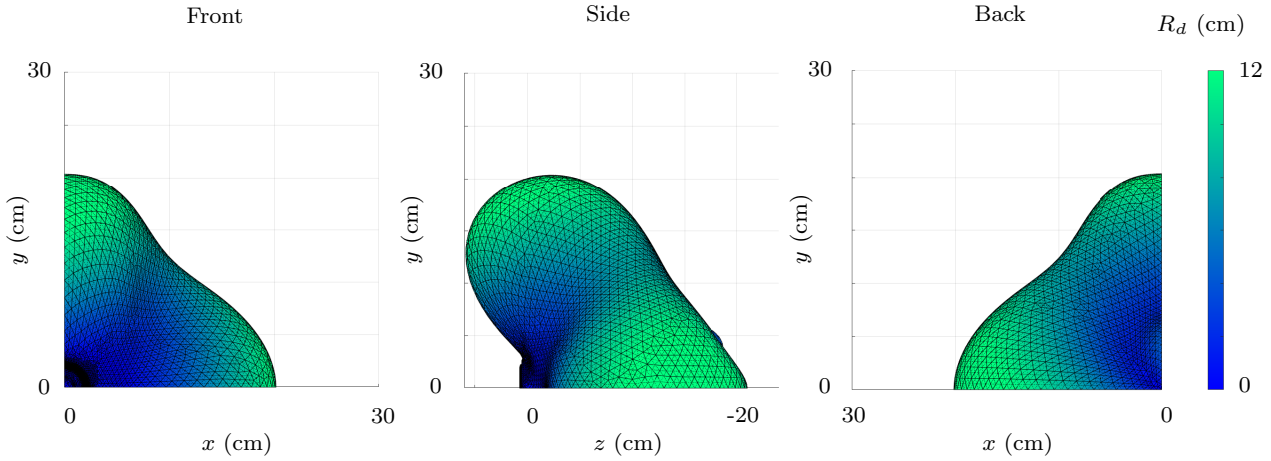


Fig. 17: The shape optimized design using the minimiax formulation with $\phi_{B,2}$. The colormap shows the distance between the nodes in the optimized mesh and the corresponding nodes in the initial non-pertubed mesh. A photo-realistic rendering of the geometry is shown in Figure 20e in the Appendix. Also, Figure 23e in the Appendix shows the location of the control points for the optimized design.

other designs.

The performance of the two optimized designs is evaluated using the cost function $\phi_k$ as a function of frequency. The plots are shown in Figures 18a and 18b. Comparing the results using equal weighting (Figure 18a) with the previous results it is observed that it is now not possible for the cost function to become zero at the three highest optimization frequencies. However, similar to the previous optimization, using an average cost function over frequency results in degraded performance at the lowest frequencies. On the other hand, the optimized design using $\phi_{B,2}$ with minimix (Figure 18b) can improve the cost function at the lowest optimization frequency. However, in this case, the cost function shows a large increase near 500 Hz ($\phi_k \approx 1$) which is e.g not observed in Figure 15c. Again the solution quickly degrades above 5 kHz and eventually becomes worse than the initial design near 6 kHz.

### 8.5 Crosscheck between the five shape optimized designs

To validate the solution of the designs using the different cost functions and optimization approaches, a crosscheck of the cost functions between the different designs is shown in Table 4. Here, the diagonal in the table should be the smallest value for individual rows. This

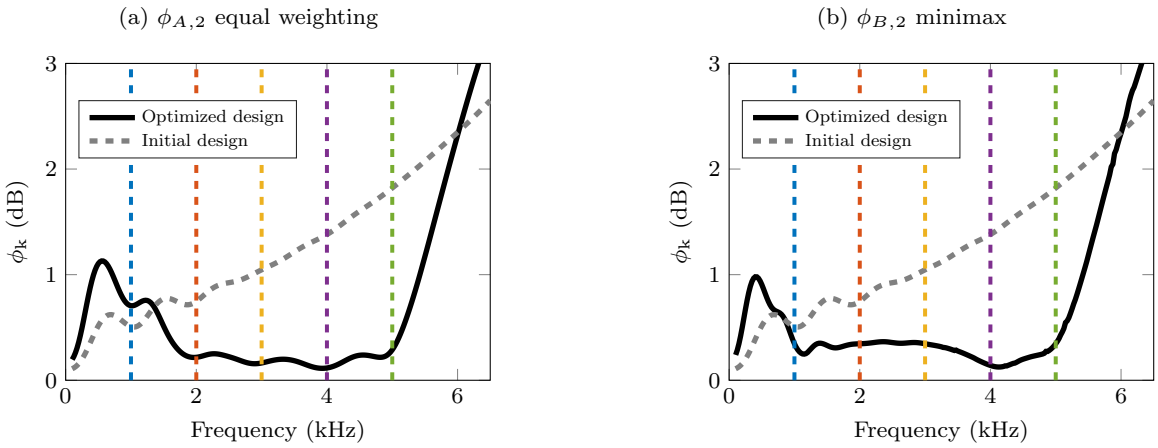


Fig. 18: The cost function $\phi_k$ as a function of frequency. In the figure, a) is the cost function evaluated for the design optimized with $\phi_{A,2}$ and equal weighting. Additionally, b) is the cost function obtaiend from the design optimized using $\phi_{B,2}$

Table 4: Crosscheck between optimized designs and individual cost functions. Individual columns correspond to a particular optimized design evaluated for the five different cost functions. Gray cells correspond to the smallest value for a particular row.

| Evaluated \ Optimized | $\phi_{A,1}$ , $w_k = 1$ | $\phi_{A,1}$ , $w_k = w_{\text{fd}}$ | $\phi_{B,1}$ | $\phi_{A,2}$ , $w_k = 1$ | $\phi_{B,2}$ |
|---|---|---|---|---|---|
| $\phi_{A,1}$ , $w_k = 1$ | 0.1891 | 0.1933 | 0.3040 | 0.2194 | 0.2169 |
| $\phi_{A,1}$ , $w_k = w_{\text{fd}}$ | 0.1770 | 0.1760 | 0.2235 | 0.1940 | 0.6876 |
| max: $\phi_{B,1}$ | 0.7247 | 0.6746 | 0.3146 | 0.6967 | 0.3265 |
| $\phi_{A,2}$ , $w_k = 1$ | 0.3201 | 0.3191 | 0.4006 | 0.2983 | 0.3048 |
| max: $\phi_{B,2}$ | 0.7361 | 0.6876 | 0.5638 | 0.7058 | 0.3460 |

ensures that a design solution optimized with a particular cost function is the best performing no matter individual cost function it is evaluated with. This indicates that the optimized design has reached a valid local minimum. The lowest value for the individual rows in the table is highlighted with gray cells. As is observed, the diagonal does indeed have the smallest values.

### 8.6 The impact of the starting guess

As is the case with any gradient based shape optimization method, one can only guarantee global optimality for convex problems, and not in the case of non-linear and non-convex problems as those being investigated in this study. In practice, this means that the solution will be highly dependent on the initial configuration. To show this, a series of three different starting guesses are created. The additional optimization studies are carried out using the cost function $\phi_{A,1}$ with equal weighting. This will explore the design sensitivity to the initial starting guess, and comment on the choice of initial configuration. The outcome of the studies is shown in Figure 19. In the figure, the three studies with different starting guesses are identified as design 1, design 2 and design 3. For design 1 and design 2 the initial design is only modified by small random perturbations of the design variables, hence, the shape is close to that of the spherical loudspeaker. It is observed that design 1 and design 2 converge to a very similar design and performance as the optimization results previously obtained for the same cost function (the design in figure 9). Hence, these local minima can be considered to be quite strong. The value of the cost function for design 1 and design 2 is $\phi_{A,1} = 0.1910$ and $\phi_{A,1} = 0.1907$, respectively. If, on the other hand, one is to start the optimization process using a significantly larger initial design the outcome is different, as can be seen in the bottom of Figure 19. For this starting guess, the optimized solution converges to a different design and also a lower value of the cost function with $\phi_{A,1} = 0.1280$, showing that the optimization results are indeed sensitive to the starting guess. Remark that the although the objective is improved, the reduction is insignificant from a practical perspective, c.f the used dB scale. Moreover, designs 1 and 2 are still more interesting: they achieve almost

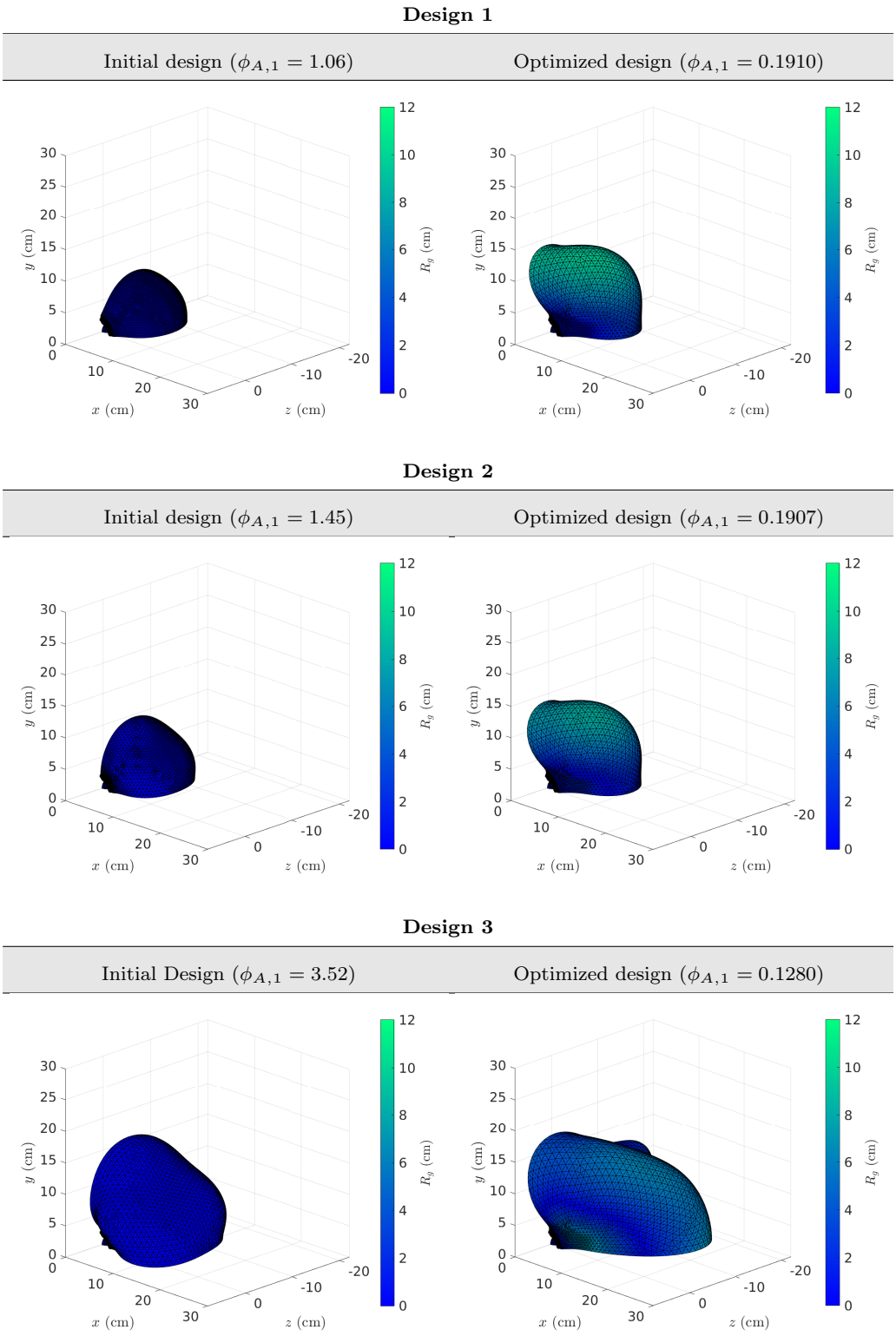


Fig. 19: Three designs obtained using different starting guesses for the initial design. The three designs are based on optimization using the cost function $\phi_{A,1}$ with equal weighting

the same result with smaller setups, which is physically more difficult given the ratio size to wavelength.

## 9 Discussion

The proposed shape optimization method demonstrates the feasibility of improving the flatness of the directivity response of a loudspeaker system by changing the shape of the cabinet. It is expected that the main acoustic effects contributing to a change in the directivity are a combination of cabinet diffraction and directivity due to a finite-sized piston. By changing the shape of the cabinet these acoustic properties can be manipulated and acoustic energy can be distributed more evenly. For this particular test case, optimization can be carried out using only five optimization frequencies and still achieve improvements inside the entire optimization band ranging from 1 to 5 kHz. This behaviour is expected to be problem-dependent and not representative for all acoustic optimization cases. In other cases, a different resolution of optimization frequencies may be required. If improvements are also desired both below and above the presented range more optimization frequencies are needed, potentially making the optimization much more expensive. This is especially the case for the upper frequency range. At higher frequencies, the design problem will be more sensitive to design changes and a much finer frequency resolution will be required. The presented results have used the same mesh density for all the frequencies and during all the optimization iterations. A suggestion to improve the computational effort of the method would be to have different meshes for different frequency ranges, which would greatly improve speed for optimization at lower frequencies where a less dense mesh is required. Additionally, a re-meshing approach could be adapted so only regions with large deformations are densely meshed. More work on the efficiency of the underlying BEM model could also be done, e.g. utilizing a model reduction method for acoustic multi-frequency BEM studies (Panagiotopoulos et al., 2020, 2021).

Perhaps not so surprisingly, it is observed that using a minimax formulation seems to be the better approach for multi-frequency optimization. Achieving similar performance using a frequency-weighted cost function might be possible. However, it will require a lot of trial and error to find the appropriate frequency weighting. A task that potentially will be very problem-dependent. In the results presented here, the weighting of lower frequencies only contributed to slightly better performance. Nonetheless, pursuing such an improved formulation is an interesting subject and will be investigated in future studies.

As typical with gradient-based optimization, the presented results are converged to local minima. A range of studies could also be performed with different starting guesses, to explore the design space and the quality of the optimized designs for all the different optimization approaches. Furthermore, there might be better cost functions to describe the directivity which could be tested in a comparative review. Additional design variables could also be added to the studies to extend the design space e.g. also using $\theta_{i,j,k}$ or $\phi_{i,j,k}$ as design variables. Also, the modelling approach and parametrization applies a quarter symmetric description of the loudspeaker; removing the constraints of symmetry could potentially lead to even better performing designs. For acoustic problems, the sensitivity to design changes will become more pronounced at higher frequencies. A possibility to improve the robustness at higher frequencies and the manufacturability would be to incorporate diluted and/or eroded design realizations into the optimization procedure. However, all such studies are considered beyond the scope and would increase the computational time required as compared to the presented work.

Another potential shortcoming is the accuracy of the underlying loudspeaker model. For many loudspeaker systems, the high-frequency behaviour is not accurately captured in the lumped parameter model. The loudspeaker unit can e.g. have break-up modes that will disturb the quality of the frequency response or directivity pattern. Moreover, the vibrations of the loudspeaker cabinet can contribute to the acoustic output of the loudspeaker, potentially creating interference effects that can degrade the loudspeaker performance. This will especially be the case for light and compact loudspeakers. To optimize considering these effects would require the inclusion of a fully coupled vibro-acoustic model. Moreover, to validate if the proposed model is sufficient would require experimental validation.

The quality of a loudspeaker system can to some extent be quantified in terms of measures like power, frequency, phase, or directivity responses. However, perceptual psycho-acoustic aspects also often determine the quality of a loudspeaker system. The perceptual quality is typically evaluated through listening tests, which are difficult to implement in a numerical optimization setting. Nevertheless, quantities like Speech Intelligibility or Perceptual Objective Listening Quality Analysis (POLQA) could perhaps be used as more

perceptual measures or cost functions (Kuttruff, 2000; Beerends et al., 2013).

## 10 Conclusions

This work has presented a method to perform gradient-based shape optimization based on FFD and semi-analytical adjoint sensitivities. The method is applied to increase the evenness of a moving coil loudspeaker system's directivity response. Performance improvements are achieved by changing the shape of the loudspeaker cabinet and minimizing a cost function describing the RMSD of the SPL in front of the loudspeaker. The studies have tested two approaches for multi-frequency optimization, namely averaging of the cost function over frequency and the minimax formulation. On the one hand, the results showcase some of the benefits of the minimax formulation, yielding a more smooth response of the cost function over several octaves. In the best-case scenario cases for this particular optimization setup, it has been possible to obtain very low values of the cost function in the optimization range from 1 to 5 kHz. On the other hand, the studies also show the difficulties of using an averaging approach combined with the more heuristic frequency weighting approach where it can be difficult to formulate an adequate frequency weighting function.

## 11 Acknowledgements

All the authors acknowledge the support of the Audio Research in GN Audio A/S and the Centre for Acoustic-Mechanical Micro Systems at the Technical University of Denmark. The work was supported by the Industrial postdoc program, Innovation Fund Denmark.

## 12 Conflict of interest

On behalf of all authors, the corresponding author states that there is no conflict of interest.

## 13 Replication of Results

The necessary information for replication of the results is presented in this paper. The interested reader may contact the corresponding author for further implementation details.

## A Renderings of the optimized designs

Photo-realistic renderings of the optimized designs are shown in the Figure 20.

## B Note on semi-analytic sensitivities and step-size

The design sensitivities are obtained from the semi-analytical adjoint approach described in Section 7 meaning that matrix design derivatives are calculated with finite differences. Therefore, the sensitivities can be dependent on the step-length. To show the sensitivity to step-length ratio, four randomly chosen design sensitivity calculations for different step-sizes are shown in Figure 21. Additionally, the semi-analytical adjoint sensitivities are compared to a pure forward finite difference sensitivity at different step-sizes. As is seen, the sensitivities are stable within the range of $10^{-5}$ to $10^{-8}$ and should therefore be chosen in this range.

## C Mesh dependency of optimized design

When performing shape optimization without any re-meshing there is the risk that the optimization becomes mesh dependent to an unacceptable degree. In such cases, the optimizer can optimize on numerical error rather than the physical effects. To study this potential mesh sensitivity, the design based on $\phi_{A,1}$ and equal weighting (the design in Figure 9) is re-meshed with a denser mesh consisting of 24002 nodes and 12000 elements. The SPL frequency response for the 0° and 70° field point is shown in Figure 22a and Figure 22b, respectively. The Figures show close to no changes in the SPL response between the mesh used during optimization and the mesh that is re-meshed with the denser mesh. Hence, it is expected that the mesh utilized during optimization can be safely used.

## D Visualization of control points for optimized designs

The location of the control points for the five optimized designs are visualized in Figure 23.

## References

Andersen, P. R., Kook, J., Henríquez, V. C. and Aage, N. (2020), 'Towards large-scale acoustic shape optimization for industrial applications using the boundary element method', *Proceedings of 2020 International Congress on Noise Control Engineering, Inter-noise, Soul, South Korea, Online* .

Andersen, P. R., Kook, J., Henríquez, V. C. and Aage, N. (2021), '3d shape optimization of loudspeakers', *Proceedings of 2021 International Congress on Noise Control Engineering, Inter-noise, Washington, United States of America, Online* .

Beerends, J. G., Schmidmer, C., Berger, J., Obermann, M., Ullmann, R., Pomy, J. and Keyhl, M. (2013), 'Perceptual objective listening quality assessment (polqa), the third

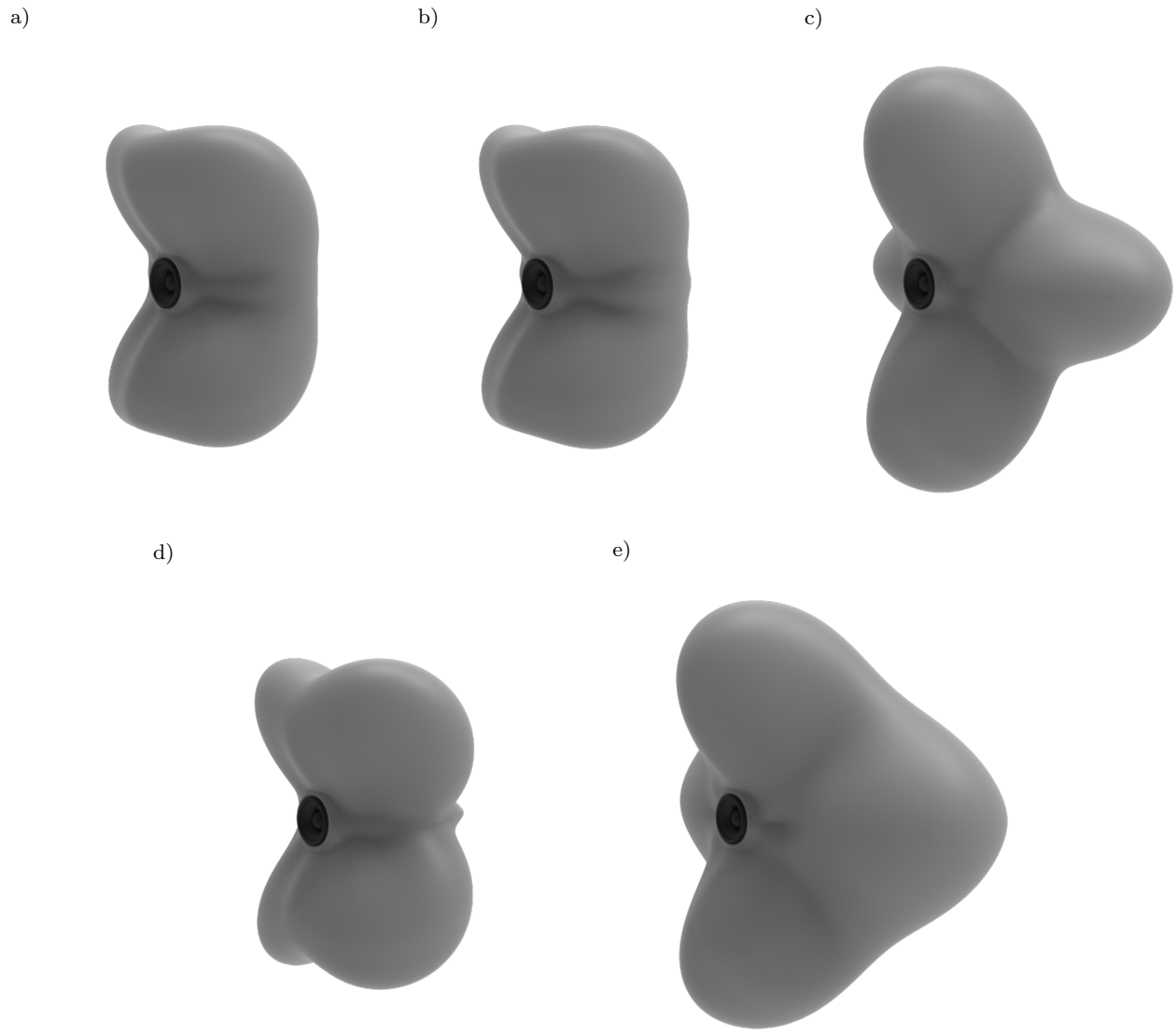


Fig. 20: Photo-realistic renderings of the optimized designs. In the Figure, a) is the design optimized with $\phi_{A,1}$ and $w_k = 1$, b) is the design optimized with $\phi_{A,1}$ and $w_k = w_{fd}$, c) is the design optimized with $\phi_{B,1}$, d) is the design optimized with $\phi_{A,2}$ amd $w_k = 1$, and e) is the design optimized with $\phi_{B,2}$. Remark that all renderings are on the same scale to illustrate the difference in size between optimized designs.

generation itu-t standard for end-to-end speech quality measurement part ii—perceptual model', *J. Audio Eng. Soc* **61**(6), 385–402.
**URL:** *http://www.aes.org/e-lib/browse.cfm?elib=16830*

Beranek, L. L. and Mellow, T. (2012), *Acoustics: Sound Fields and Transducers*, Elsevier Inc.

Bezzola, A. (2018), 'Numerical optimization strategies for acoustic elements in loudspeaker design', *145th Audio Engineering Society International Convention, Aes 2018* .

Bängtsson, E., Noreland, D. and Berggren, M. (2003), 'Shape optimization of an acoustic horn', *Computer Methods in Applied Mechanics and Engineering* **192**(11-12), 1533–1571.

Bücklein, R. (1981), 'The audibility of frequency response irregularities', *J. Audio Eng. Soc* **29**(3), 126–131.
**URL:** *http://www.aes.org/e-lib/browse.cfm?elib=10291*

Christensen, R. (2020), 'Shape and topology optimization of loudspeaker drivers', *Proceedings from COMSOL Conference, Grenoble/Online* .

Creixell Mediante, E., Jensen, J. S., Naets, F., Brunskog, J. and Larsen, M. (2018), 'Adaptive parametric model order reduction technique for optimization of vibro-acoustic models: Application to hearing aid design', *Journal of Sound and Vibration* **424**, 208–223.

Dilgen, C. B. and Aage, N. (2021), 'Generalized shape optimization of transient vibroacoustic problems using cut elements', *International Journal for Numerical Methods in Engineering* **122**(6), 1578–1601.

Dilgen, S. B., Jensen, J. S. and Aage, N. (2021), 'Shape optimization of the time-harmonic response of vibroacoustic

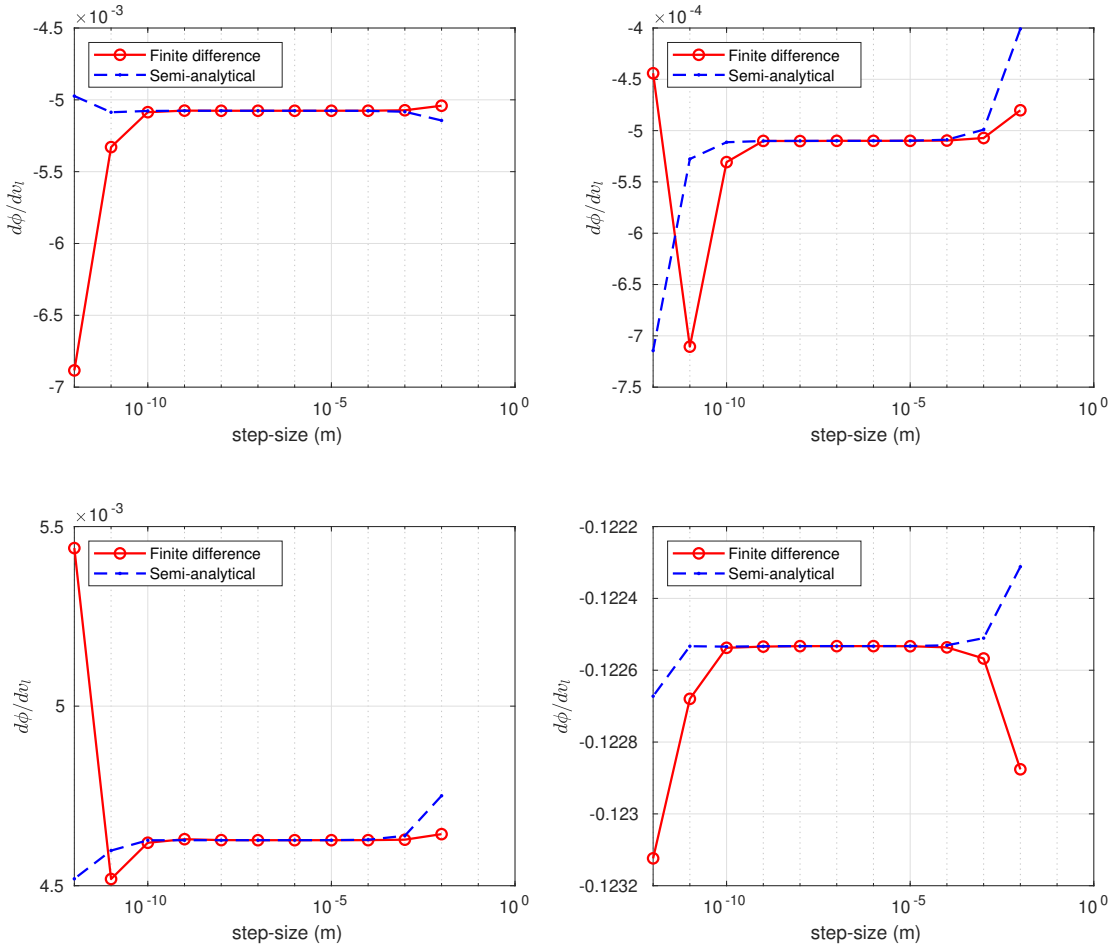


Fig. 21: A set of four randomly chosen design sensitivities based on the frequency averaged cost function calculated for different step-lengths. The sensitivities are both calculated with the semi-analytical adjoint approach (blue) and a forward finite difference scheme (red). The sensitivities are calculated for the initial design.

devices using cut elements', *Finite Elements in Analysis and Design* **196**, 103608.

Dühring, M. B., Jensen, J. S. and Sigmund, O. (2008), 'Acoustic design by topology optimization', *J. Sound Vib.* **317**, 557–575.

Evans, W., Dyreby, J., Bech, S., Zielinski, S. and Rumsey, F. (2009), 'Effects of loudspeaker directivity on perceived sound quality - a review of existing studies', *126th Audio Engineering Society Convention 2009* **1**, 221–229.

Jensen, J. S. and Sigmund, O. (2005), 'Topology optimization of photonic crystal structures: a high-bandwidth low-loss t-junction waveguide', *Journal of the Optical Society of America B* **22**(6), 1191–1198.

Juhl, P. M. and Henríquez, V. C. (2010), 'Openbem - an open source boundary element method software in acoustics', *Proceedings Internoise 2010, Lisbon, Portugal* .

Juul-Nyholm, H. B., Severinsen, J. C., Schneider, H., Mortensen, N. H. and Andersen, M. A. E. (2017), Construction of lightweight loudspeaker enclosures, *in* 'Audio Engineering Society Convention 142'.
**URL:** *http://www.aes.org/e-lib/browse.cfm?elib=18660*

Kates, J. M. (1979), 'Loudspeaker cabinet reflection effects', *J. Audio Eng. Soc* **27**(5), 338–350.
**URL:** *http://www.aes.org/e-lib/browse.cfm?elib=3202*

Khajah, T., Liu, L., Song, C. and Gravenkamp, H. (2021), 'Shape optimization of acoustic devices using the scaled boundary finite element method', *Wave Motion* **104**, 102732.

Kinsler, L. E. (2000), *Fundamentals of acoustics*, Wiley.

Kuttruff, H. (2000), *Room acoustics*, 4th edn, Spon Press, London.

Leach, W. M. (2010), *Introduction to electroacoustics & audio amplifier design*, Kendall Hunt, Dubuque, IA.

Linkwitz, S. (2002), Which loudspeaker parameters are important to create the illusion of a live performance in the living room?, *in* 'Audio Engineering Society Convention 113'.
**URL:** *http://www.aes.org/e-lib/browse.cfm?elib=11289*

Marburg, S. and Nolte, B. (2008), *Computational acoustics of noise propagation in fluids -Finite and boundary element*

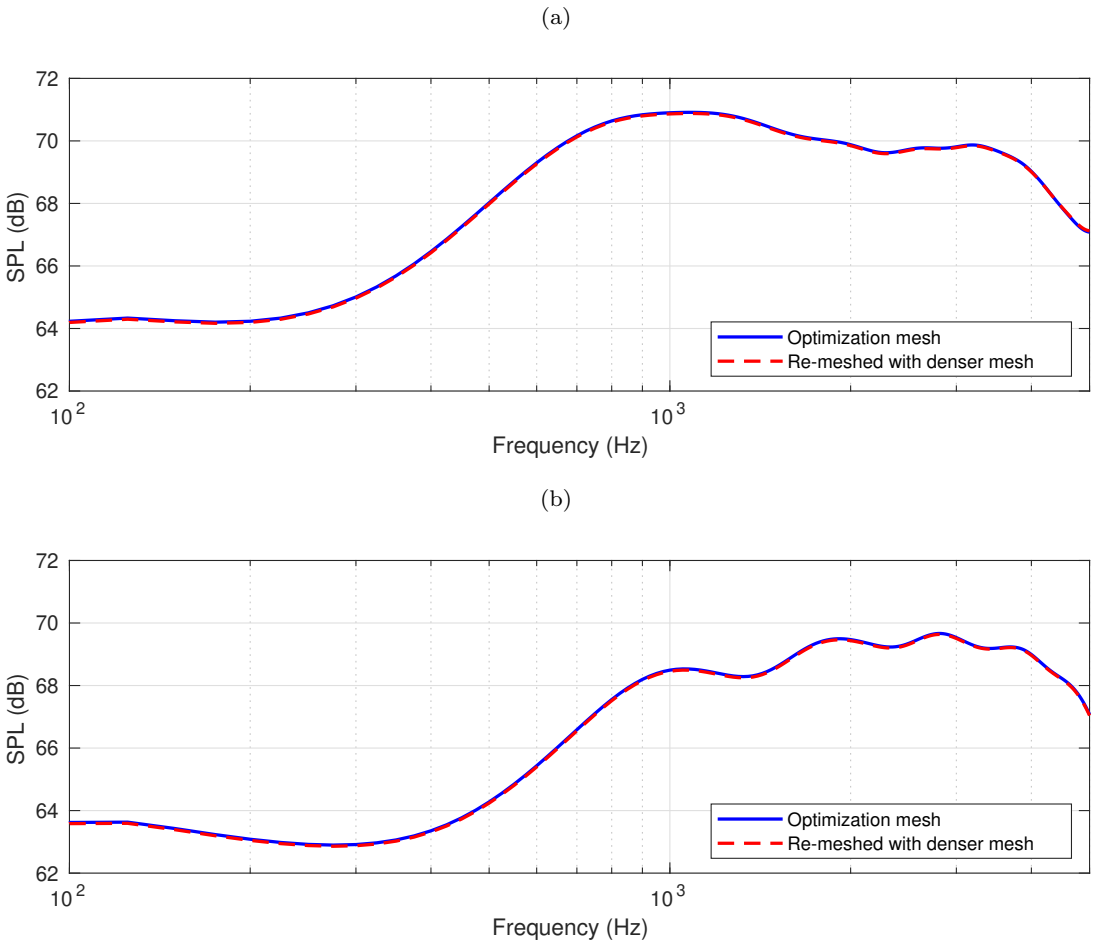


Fig. 22: The SPL frequency response based on the optimized design in Figure 9 using the cost function $\phi_{A,1}$ with equal weighting. In the figure, a) is calculated at $\psi = 0°$ and b) is calculated at $\psi = 70°$. The blue curves are calculations based on the mesh used during optimization and the red curves are re-meshed with a denser mesh using 24002 nodes and 12000 elements

*methods*, Springer Berlin Heidelberg.

Matsumoto, T., Yamada, T., Takahashi, T., Zheng, C. J. and Harada, S. (2011), 'Acoustic design shape and topology sensitivity formulations based on adjoint method and bem', *Computer Modeling in Engineering and Science* **78**(2), 77–94.

Nielsen, D. G., Agerkvist, F. T. and Jensen, J. S. (2021), 'Achieving a flat, wideband frequency response of a loudspeaker unit by numerical optimization with requirements on its directivity', *Journal of the Acoustical Society of America* **150**(2), 663–672.

Nielsen, D. G., Andersen, P. R., Jensen, J. S. and Agerkvist, F. T. (2020), 'Estimation of optimal values for lumped elements in a finite element - lumped parameter model of a loudspeaker', *Journal of Computational Acoustics* **28**(2), 2050012.

Olson, H. F. (1951), 'Direct radiator loudspeaker enclosures'.

Panagiotopoulos, D., Deckers, E. and Desmet, W. (2020), 'Krylov subspaces recycling based model order reduction for acoustic bem systems and an error estimator', *Computer Methods in Applied Mechanics and Engineering* **359**, 112755.

Panagiotopoulos, D., Desmet, W. and Deckers, E. (2021), 'An automatic krylov subspaces recycling technique for the construction of a global solution basis of non-affine parametric linear systems', *Computer Methods in Applied Mechanics and Engineering* **373**, 113510.

Panzer, J. (2012), Coupled lumped and boundary element simulation for electro-acoustics, *in* 'Proceedings of the Acoustics 2012 Nantes Conference'.

Queen, D. (1979), 'Effect of loudspeaker radiation patterns on stereo imaging and clarity', *J Audio Eng Soc* **27**(5), 368–379.

Schmidt, S., Wadbro, E. and Berggren, M. (2016), 'Large-scale three-dimensional acoustic horn optimization', *Siam Journal on Scientific Computing* **38**(6), B917–B940.

Sederberg, T. (1986), 'Free-form deformation of solid geometric models', *Computer Graphics,Volume 20, Issue 4, pp 151-60* .

Seybert, A. F., Soenarko, B., Rizzo, F. J. and Shippy, D. J. (1985), 'An advanced computational method for radiation and scattering of acoustic waves in three dimensions', *Journal of the Acoustical Society of America* **77**(2), 362–368.

Small, R. H. (1971), 'Direct-radiator loudspeaker system analysis', *Ieee Transactions on Audio and Electroacoustics* **AU-19**(4), 269–281.

T. Christensen, S. and Olhoff, N. (1998), 'Shape optimization of a loudspeaker diaphragm with respect to sound directivity properties', *Control and Cybernetics* **27**(2).

Udawalpola, R. and Berggren, M. (2008), 'Optimization of an acoustic horn with respect to efficiency and directivity', *Int J Numer Methods Eng* **73**(11), 1571–1606.

Udawalpola, R., Wadbro, E. and Berggren, M. (2011), 'Optimization of a variable mouth acoustic horn', *Int J Numer Methods Eng* **85**(5), 591–606.

Wright, J. (1998), Finite element analysis as a loudspeaker design tool, *in* 'Audio Engineering Society Conference: UK 13th Conference: Microphones & Loudspeakers'.
**URL:** *http://www.aes.org/e-lib/browse.cfm?elib=7992*

Wu, T. W. (2000), *Boundary element acoustics : fundamentals and computer codes*, WIT.

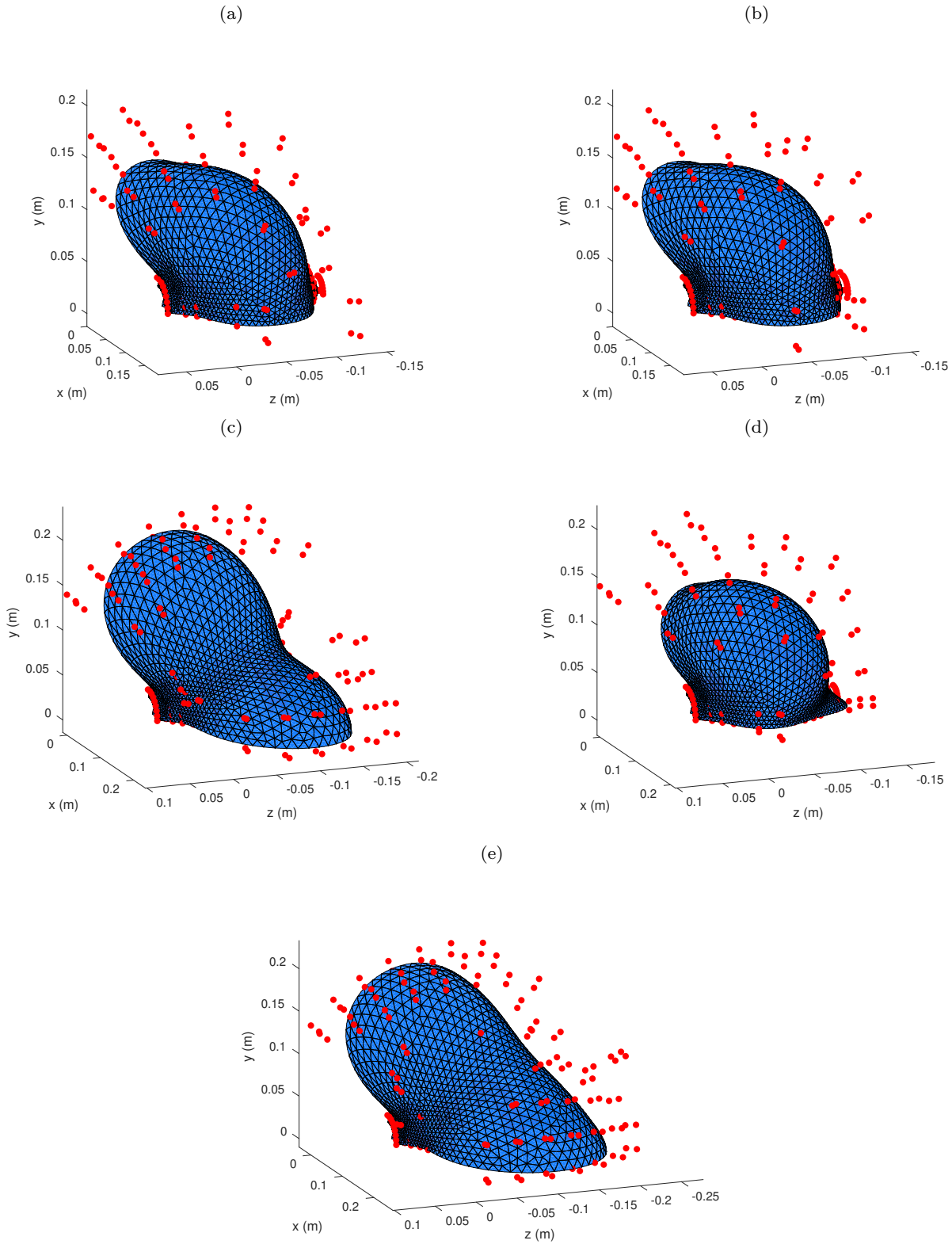


Fig. 23: The geometry of the optimized designs including the control points. In the figure, a) is the optimized design using $\phi_{A,1}$ and $w_k = 1$, b) is the design using $\phi_{A,1}$ and $w_k = w_{fd}$, c) is design using $\phi_{B,1}$, d) is the design using $\phi_{A,2}$ and $w_k = 1$, and e) is the design using $\phi_{B,2}$.